Vibronic Resonances Arising from Conically Intersecting Electronic States

Ronald S. Friedman* and Iwona Podzielinski

Department of Chemistry, Indiana University Purdue University Fort Wayne, Ft. Wayne, Indiana 46805-1499

Lorenz S. Cederbaum†

Theoretische Chemie, Physikalisch-Chemisches Institut Universität Heidelberg, D-6900 Heidelberg, Federal Republic of Germany

Victor M. Ryaboy‡ and Nimrod Moiseyev‡

Department of Chemistry and Minerva Center for Non Linear Physics, Technion - Israel Institute of Technology, Haifa 32000, Israel

Received: October 3, 2001; In Final Form: February 6, 2002

We provide here a quantum mechanical investigation of the resonance states found in a study of conically intersecting electronic surfaces. The dynamical system under investigation consists of a bound electronic state having a conical intersection with a dissociative electronic state. Quantum mechanical resonances arise from the predissociation of vibrational states of the bound potential surface via the nonadiabatic coupling to the dissociative potential surface. Resonance energies and wave functions are computed using the complex coordinate method, and the resonances are characterized in terms of contributions from states of the uncoupled potential surfaces. Key results found in this study include the following: (i) there is no correlation between resonance positions and widths in that when the resonances are ordered by their positions, the corresponding widths (and lifetimes) fluctuate irregularly; (ii) the resonance energetically below the conical intersection cannot be identified as a tunneling resonance of the lowest adiabatic potential surface since its resonance lifetime is orders of magnitude larger than the tunneling lifetime; (iii) the resonance states (even those whose positions are energetically much higher than the conical intersection) are found to arise from a small number of vibrational states of the bound diabat coupling to each other via the continuum of the dissociative diabat; and (iv) none of the resonance states emanate from a bound state of the upper adiabatic cone-shaped potential surface. We also briefly investigate the resonance energies as a function of the nonadiabatic coupling strength; the irregular behavior of the resonance lifetimes with the coupling strength is a fingerprint of the conical intersection. Furthermore, we have performed a symmetry analysis of the resonances and introduced an effective Hamiltonian which, with the aid of a simple model, yields results in agreement with numerically exact results.

I. Introduction

The Born−Oppenheimer approximation[1] is of fundamental importance in the study of many dynamical processes. Within this approximation, the electronic problem is first solved at fixed nuclear geometries, yielding a potential energy surface (PES); the motion of the nuclei on the PES is then treated. For many dynamical systems, nuclear motion is confined to a single potential surface, often the surface associated with the electronic ground state of the system. However, "nonadiabatic" processes for which nuclear motion "evolves" on or is influenced by several coupled potential surfaces are in fact ubiquitous (see, for examples, refs 2−6 and refs therein.)

Considerable research has been undertaken to understand nonadiabatic effects in model one-dimensional systems in which two adiabatic potential energy curves can undergo an avoided crossing. Notable is the work of Nakamura and collaborators,[7] who have made tremendous strides in extending the pioneering work of Landau and Zener.[8] The role of quasibound states, i.e. quantum mechanical resonances, in model one-dimensional electronically nonadiabatic reactions has also been investigated.[9] In systems with only one internal degree of freedom, Born−Oppenheimer (adiabatic) potential energy surfaces of the same spatial symmetry cannot intersect. However, in dynamical systems possessing N internal degrees of freedom, it is possible that adiabatic PES intersect along a generalized line of dimension $N - 2$.[2−6] Thus, two-dimensional potential surfaces, which can intersect at a point, present the lowest dimensionality necessary for a so-called conical intersection.

The simplest system that is a generalization of the one-dimensional, two-state Landau−Zener model and that involves a conical intersection is the motion of a point-mass particle across a pair of coupled two-dimensional PES with particle motion constrained to a plane generating the hyperbolic conical section. Such a system displays metastable states (resonances) that are supported by a conical potential well that is coupled to a conical peak; a semiclassical analysis of the resonance cone

* To whom correspondence should be addressed. E-mail: friedman@hilbert.ipfw.edu Fax: (260) 481-6070.
† E-mail: Lorenz.Cederbaum@urz.uni-heidelberg.de.
‡ E-mail: chr05vr@techunix.technion.ac.il nimrod@techunix.technion.ac.il..

10.1021/jp0136922 CCC: $22.00 © 2002 American Chemical Society
Published on Web 04/10/2002

states has resulted in explicit analytical expressions for resonance positions and widths.[10]

The effects of conical intersections between *bound* electronic states have undergone numerous theoretical investigations.[2,11,12] The studies range from investigations on small molecules such as NO_2,[12] for which the ground state conically intersects an excited state resulting in a very complex experimental absorption spectrum,[13] to larger systems such as pyrazine where the effect of all 24 modes have been computed via wave packet propagation.[14] Since resonance states, i.e. decaying states, are the subject of the present work, we would like to mention for completeness that conical intersections can have a dramatic impact on the radiative lifetimes of vibronic states.[15]

Conical intersections involving *dissociative* or continuum electronic states are also critically important, for example in the nonadiabatic effects accompanying the photodissociation of polyatomic molecules.[2−6] Numerous experimental and theoretical studies have been undertaken that provide strong evidence for the critical role of nonadiabaticity in photodissociation dynamics, including studies of ammonia and its methyl-substituted derivatives;[16] acetyl, bromoacetyl and bromopropionyl chloride;[17] nitric oxide;[18] nitrous oxide;[19] dinitrogen tetraoxide;[20] monohalogen and multihalogen alkyl halides;[21] *tert*-butyl nitrite;[22] metal carbonyls;[23] H_2O and its deuterated analogues;[24] OClO;[25] ICN;[26] HCO;[27] OH−H_2[28] and Ar−H_2O[29] van der Waals complexes; the CH_2OH radical[30] and NO dimer;[31] HNCO;[32] and O_3.[33]

One important nonadiabatic mechanism for photodissociation in polyatomics involves photoabsorption from the ground electronic state to a bound electronically excited state which conically intersects a dissociative excited state. Time-dependent wave packet calculations have been utilized for CH_2[34] and H_2S[35] using the ground and two excited potential surfaces to compute photodissociation cross-sections and product branching ratios; theoretical and experimental results for both molecular systems are in good agreement. The computed cross-sections provide strong evidence for the existence of resonances; the latter arise from levels of the bound excited PES which are predissociated via the nonadiabatic coupling to the dissociative PES. A time-dependent wave packet study was also undertaken for the photoionization of HCN[36] in which the resultant HCN^+ molecular ion dissociates due to a conical intersection between a bound and repulsive electronic state; time-dependent populations of diabatic and adiabatic electronic states were computed.

Although the effects of resonances were observed in the above wave packet investigations, detailed analyses of the resonances (e.g., calculations of positions, widths and wave functions of resonance states) were not undertaken. To provide such an analysis of the resonances resulting from a conical intersection between a bound and dissociative PES, we present below a quantum mechanical investigation of conically intersecting electronic states, analyzing the resonances arising in such a system using the complex coordinate method. Since at least two degrees of freedom are required to have a conical intersection and because this investigation of resonances arising from a conical intersection is the first such study of its kind, we focus on a two-coordinate system.

We would like to mention that the complex coordinate method has been previously used[37] in connection with a conical intersection, in particular a linear Jahn−Teller system in which two adiabatic surfaces occur one inside the other and are connected by a point of conical intersection. In a bound linear Jahn−Teller system the vibrational states in the upper adiabatic potential surface (cone states) couple to those of the lower surface. By appropriately using the complex coordinate method the authors of ref 37 computed decay rates of the cone states mediated by this coupling.

In section II, we provide the theoretical formalism for the analysis of resonance states; results are presented in section III. In section IV, we discuss the symmetry of the resonance states which is decisive for a detailed description of the resonances. Also in this section, a method of analysis is provided by the introduction of an effective Hamiltonian; with the aid of this Hamiltonian a simple model can be derived to help provide valuable insight into understanding the resonance results. Section V gives concluding remarks.

II. Resonance States: Complex Scaling Characterization

A. Electronic States and the Potential Matrix. The simplest type of conical intersection arises from two nondegenerate electronic states of different symmetries interacting through a nontotally symmetric mode, whereas, in addition, a totally symmetric mode regulates the separation in energy of the interacting states.[2] In accord with this form for the conical intersection, we undertake here a reduced-dimensionality quantal study of two conically intersecting diabatic electronic states whose potential energy surfaces depend on two dimensionless normal-mode coordinates, x (a symmetric coordinate) and y (an asymmetric coordinate). One diabatic electronic state, denoted Φ_b, is bound in both coordinates and is associated with the potential V_b^d. The other diabatic electronic state, denoted Φ_c, is bound in y and dissociative in x; it is associated with the potential V_c^d. The electronic states are coupled via the potential V_{bc}^d. The quantum dynamics is solved in the diabatic representation; however, in section III.C below, we will also use the adiabatic potential energy surfaces to help interpret the resonance results.

The diabatic potential energy matrix is therefore given by

$$V^d(x,y) = \begin{pmatrix} V_b^d & V_{bc}^d \\ V_{bc}^d & V_c^d \end{pmatrix} \tag{1}$$

The vibrational states of V_b^d are predissociated via the nonadiabatic coupling V_{bc}^d to the dissociative V_c^d resulting in the appearance of resonance states. The diabatic potential matrix gives rise to conically intersecting electronic states; if we imagine that both Φ_b and Φ_c represent *excited* electronic states, then the dynamical system is a model for molecular photodissociation in which photon absorption from a ground electronic state results in predissociation from excited states undergoing a conical intersection.

A potential energy matrix as in eq 1 is applicable to realistic cases and can easily be generalized to more dimensions. In this first study we consider here a simple form for V^d given by

$$V_b^d(x,y) = \frac{1}{2}\omega_x x^2 + \frac{1}{2}\omega_y y^2 \tag{2a}$$

$$V_c^d(x,y) = \epsilon\, e^{-\beta(x+\delta)} + \frac{1}{2}\omega_y y^2 + \Delta \tag{2b}$$

$$V_{bc}^d(y) = \lambda\, y \tag{2c}$$

The coupling V_{bc}^d is chosen for clarity and simplicity to be a linear function of the coupling mode y as in previous models of electronic coupling.[2,38] The potential parameters are given in Table 1; we use atomic units unless otherwise indicated. The parameters have been chosen by comparison to model systems

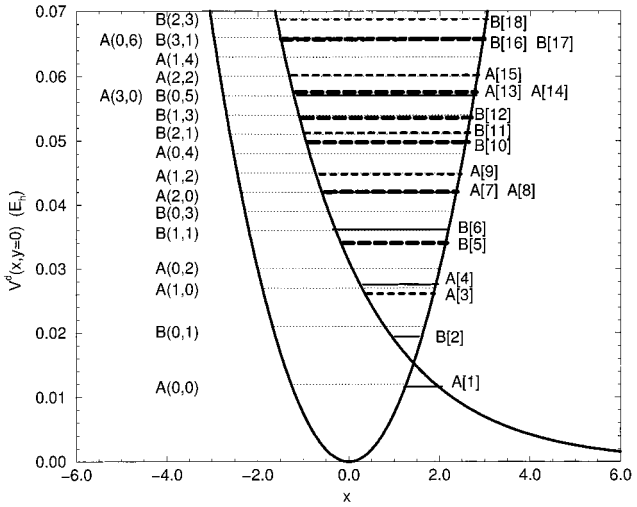

Figure 1. Bound diabatic V_b^d and dissociative diabatic V_c^d potentials at $y = 0$ as functions of x. The energies of the vibrational levels (n_x, m_y) of $V_b^d(x, y)$ are indicated by horizontal dotted lines; some of the unperturbed levels are doubly degenerate. The positions E_α of the resonances are indicated by horizontal solid lines (Group 1), thicker dashed lines (Group 2) and thickest long-dashed lines (Group 3). The placement of the horizontal lines representing the resonance positions is chosen only for convenience; i.e., the resonances are not localized inside the upper adiabatic cone and do not result from cone states. The symmetry (*A* or *B*) of the vibrational states and the resonances is shown as well as the number [α] of the resonance state.

TABLE 1: Values of Potential Energy Parameters

$\omega_x = 0.015$
$\omega_y = 0.009$
$\epsilon = 0.04$
$\beta = 0.5$
$\delta = 0.5$
$\Delta = 0$
$\lambda = 0.005$[a]

[a] Other values are considered in section III. D.

in the literature.[36] The choice for the potential energy matrix (1) provides us with a model simple enough that we can clearly study the effects of conical intersections on resonances.

Cuts of the diabatic potentials V_b^d and V_c^d at $y = 0$ are shown in Figure 1. For the potential parameters given, the conical intersection occurs at the point ($x_{CI} = 1.427$, $y_{CI} = 0$) with an energy $E_{CI} = 0.01526$ au. The bound surface V_b^d supports harmonic vibrational states which we denote $|n_x, m_y>$ and although the vibrational energies are given simply by

$$E_{bnd} = E_{n_x} + E_{m_y} = \left(n_x + \frac{1}{2}\right)\omega_x + \left(m_y + \frac{1}{2}\right)\omega_y \qquad (3)$$

we list the first 22 vibrational levels in Table 2 for future reference. The energies of the vibrational states up to 0.07 au are indicated in Figure 1. The dissociative surface V_c^d "supports" states $|E_j, i_y>$ where $|E_j>$ is a continuum state in the x-coordinate and $|i_y>$ is a harmonic vibrational state in the y-coordinate.

B. Complex Scaled Hamiltonian. Within the basis of the two diabatic electronic states, the Hamiltonian for nuclear motion takes the form

$$\mathbf{H}(x, y) = \begin{pmatrix} H_b & V_{bc}^d \\ V_{bc}^d & H_c \end{pmatrix} \qquad (4)$$

where H_b is the nuclear Hamiltonian for the bound diabatic state Φ_b and H_c for the continuum diabatic state Φ_c. The complex

TABLE 2: Vibrational Energy Levels for States $|n_x, m_y>$ of V_b^d

n_x	m_y	E_{bnd} (E_h)	n_x	m_y	E_{bnd} (E_h)
0	0	0.012	0	5	0.057
0	1	0.021	3	0	0.057
1	0	0.027	2	2	0.060
0	2	0.030	1	4	0.063
1	1	0.036	0	6	0.066
0	3	0.039	3	1	0.066
2	0	0.042	2	3	0.069
1	2	0.045	1	5	0.072
0	4	0.048	4	0	0.072
2	1	0.051	0	7	0.075
1	3	0.054	3	2	0.075

scaled Hamiltonian $\mathbf{H}_\theta$ is obtained[39] by scaling the dissociative coordinate x via $x \rightarrow \tilde{x}$ where

$$\tilde{x} = (x - x_0)\exp(i\theta) + x_0 \qquad (5)$$

The complex scaled square-integrable (diabatic) resonance wave functions are associated with the eigenfunctions of $\mathbf{H}_\theta$

$$\mathbf{H}_\theta\, \Psi_{res_\alpha}^\theta(x, y) = \left(E_\alpha - \frac{i}{2}\Gamma_\alpha\right)\Psi_{res_\alpha}^\theta(x, y) \qquad (6)$$

where E_α and Γ_α are, respectively, the resonance position and width for the resonance labeled α. The width is inversely related to the lifetime of the resonance state. The complex scaled Hamiltonian can be further written as

$$\mathbf{H}_\theta = T\mathbf{1} + V^d(\tilde{x}, y) \qquad (7)$$

where

$$T = T(\tilde{x}) + T(y) = -\frac{1}{2}\omega_x \exp(-2i\theta)\frac{\partial^2}{\partial x^2} - \frac{1}{2}\omega_y \frac{\partial^2}{\partial y^2} \qquad (8)$$

The diabatic resonance wave function is a column vector given by

$$\Psi_{res_\alpha}^\theta = \begin{pmatrix} \Psi_{b_\alpha}^\theta \\ \Psi_{c_\alpha}^\theta \end{pmatrix} \qquad (9)$$

where $\Psi_{b_\alpha}^\theta$ is the component associated with the bound surface V_b^d and $\Psi_{c_\alpha}^\theta$ is the component associated with the continuum surface V_c^d.

C. Computational Considerations: Basis Sets. We describe details for the computation of resonance energies and wave functions. The basis sets chosen for the solution of eq 6 are particularly well-suited for determining the percent contributions from individual vibrational levels of the (uncoupled) PES V_b^d and V_c^d to the resonance state.

In the first step, we consider the bound coordinate y. A set of particle-in-a-box basis set functions (centered at $y = 0$) are used to compute eigenfunctions for the y-dependent part of H_b [i.e., for $T(y) + V_b^d(x = 0, y)$] and then for the y-dependent part of H_c [i.e., for $T(y) + V_c^d(x = 0, y)$]. These (real harmonic oscillator) eigenfunctions are denoted $Y_{1m}(y)$ and $Y_{2i}(y)$, respectively; they correspond to the states $|m_y>$ and $|i_y>$ respectively. Values for the numerical parameters n_{bas} (the number of basis-set functions) and y_{box} (the box size in y) must be specified.

In the second step, we consider the dissociative coordinate x and choose values of x_0 and the rotation angle θ to specify $\tilde{x}$ in eq 5. We then use the n_{bas} particle-in-a-box basis functions to find the eigenfunctions for the x-dependent part of the complex

scaled H_b^θ [i.e., for $T(\tilde{x}) + V_b{}^d(\tilde{x}, y = 0)$] and then for the x-dependent part of the complex scaled H_c^θ [i.e., for $T(\tilde{x}) + V_c{}^d(\tilde{x}, y = 0)$]. We denote the eigenfunctions $X_{1n}^\theta(\tilde{x})$ and $X_{2j}^\theta(\tilde{x})$, respectively; the former represents a (complex scaled) harmonic oscillator state $|n_x^\theta>$ and the latter a rotated continuum state $|E_j^\theta>$. The box size $x_{box} = x_{max} - x_{min}$ must be specified; the basis functions are centered in the middle of the box.

We then form the set of eigenfunctions of the complex scaled H_b^θ, which is given by the products $(X_{1n}^\theta Y_{1m})$; these are the eigenfunctions associated with the (uncoupled) PES $V_b{}^d(\tilde{x}, y)$. Similarly, the set $(X_{2j}^\theta Y_{2i})$ is a set of the eigenfunctions of the complex scaled H_c^θ associated with the (uncoupled) PES $V_c{}^d(\tilde{x}, y)$.

A basis for the full complex scaled Hamiltonian $\mathbf{H}_\theta$ is then taken to be a subset of the $(X_{1n}^\theta Y_{1m})$ and $(X_{2j}^\theta Y_{2i})$ functions. This subset is chosen using an energy cutoff criterion; all eigenfunctions of H_b^θ and H_c^θ whose eigenvalues have real parts which do not exceed E_{cut} are included in the basis for $\mathbf{H}_\theta$.

Upon evaluating its matrix elements, we diagonalize the complex scaled Hamiltonian matrix using the routine described in ref 40, yielding resonance eigenvalues and eigenfunctions. We then ensure that resonance results are converged with respect to the numerical parameters described above.

D. Contributions to Resonance Eigenfunctions in the Diabatic Representation. In the diabatic representation the resonance state wave function has two components which are linear combinations of the eigenfunctions of the two uncoupled diabatic PES

$$\Psi_{b_\alpha}^\theta = \sum_{nm} c_{nm_\alpha} X_{1n}^\theta Y_{1m} \tag{10a}$$

$$\Psi_{c_\alpha}^\theta = \sum_{ji} d_{ji_\alpha} X_{2j}^\theta Y_{2i} \tag{10b}$$

where the coefficients c_{nm_α} and d_{ji_α} are obtained via the matrix diagonalization and the resonance state wave function is initially normalized such that

$$\sum_{nm} c_{nm_\alpha}^2 + \sum_{ji} d_{ji_\alpha}^2 = 1 \tag{11}$$

With $\Psi_{res_\alpha}^\theta$ re-normalized such that

$$\sum_{nm} |c_{nm_\alpha}|^2 + \sum_{ji} |d_{ji_\alpha}|^2 = 1 \tag{12}$$

we now define the percent populations of resonance state α on the two diabatic PES

$$P_{b_\alpha}^d = \sum_{nm} |c_{nm_\alpha}|^2 \times 100\% \tag{13a}$$

and

$$P_{c_\alpha}^d = \sum_{ji} |d_{ji_\alpha}|^2 \times 100\% \tag{13b}$$

Furthermore, we can also determine the percent contributions to the resonance states from *individual* vibrational states of the uncoupled diabatic PES. In particular, $V_b{}^d$ supports vibrational states $|n_x, m_y>$ which make a percent contribution to resonance state α of

$$P_{b_\alpha}^{n_x,m_y} = |c_{nm_\alpha}|^2 \times 100\% \tag{14}$$

The dissociative $V_c{}^d$ PES supports states $|E_j, i_y>$; the total percent contribution to resonance α from a given vibrational state $|i_y>$ in the bound y dimension is obtained by summing over the discrete set of rotated continuum states $|E_j^\theta>$

$$P_{c_\alpha}^{i_y} = \sum_j |d_{ji_\alpha}|^2 \times 100\% \tag{15}$$

This latter probability is experimentally significant because it is related to the probability that the molecular photodissociation process results in a particular vibrational level of one of the resulting fragments.

E. Contributions to Resonance Eigenfunctions in the Adiabatic Representation. The resonance wave function was computed above using the diabatic representation. We would also like to discuss the resonances in connection with the commmon adiabatic potential energy surfaces as obtained from the ab initio calculations of electronic energies. The adiabatic potential energy matrix V^{ad} is obtained by diagonalizing the diabatic potential matrix of eq 1

$$V^{ad}(x, y) = U^T(x, y)\, V^d(x, y)\, U(x, y) \tag{16}$$

where

$$V^{ad}(x, y) = \begin{pmatrix} V_l^{ad} & 0 \\ 0 & V_u^{ad} \end{pmatrix} \tag{17}$$

and

$$U(x, y) = \begin{pmatrix} \cos\phi & -\sin\phi \\ \sin\phi & \cos\phi \end{pmatrix} \tag{18}$$

with

$$\phi(x, y) = -\frac{1}{2} \arctan\left(\frac{2V_{bc}^d}{V_c{}^d - V_b{}^d}\right) \tag{19}$$

The lower adiabatic PES V_l^{ad} resembles $V_b{}^d$ at points (x, y) with $x < x_{CI}$ and it resembles $V_c{}^d$ at points (x, y) with $x > x_{CI}$. It is a dissociative PES which itself can support continuum states and, perhaps, resonance states. The upper adiabatic PES V_u^{ad} resembles $V_c{}^d$ at points (x, y) with $x < x_{CI}$ and it resembles $V_b{}^d$ at points (x, y) with $x > x_{CI}$. It is a cone-shaped PES which, ignoring potential coupling, supports bound states which will be denoted $\chi_k(x, y)$.

We do not intend to recompute the resonance energies and eigenfunctions via complex rotation of the Hamiltonian in the adiabatic representation into the complex energy plane. We are rather interested in projecting the computed resonance eigenfunctions in the diabatic representation on the adiabatic electronic states. In this way, we can interpret the results we have obtained above in the common context of adiabatic potential surfaces. The resulting square-integrable projected resonance state wave function is obtained from the complex scaled resonance wave function in the diabatic representation (renormalized according to eq 12) via

$$F_{res_\alpha}^\theta(x, y) = U^T(x, y)\Psi_{res_\alpha}^\theta(x, y) \tag{20}$$

and consists of a component $F_{l_\alpha}^\theta(x, y)$ on the dissociative lower adiabatic PES and a component $F_{u_\alpha}^\theta(x, y)$ on the bound upper adiabatic PES. By computing the overlaps of $F_{u_\alpha}^\theta$ with the (complex scaled) bound states χ_k^θ, we can determine the percent population of the resonance state α on the upper

TABLE 3: Values of Numerical Parameters Used for Convergence of Resonance Energies

parameter	production run	convergence run
n_{bas}	500	450, 550
y_{box}	20	18
x_{max}	14	13, 14.5
x_{min}	−8	−7
E_{cut}	0.15	0.16
x_0	0	0.5
θ^a	0.20	0.15, 0.30
θ^b	0.35	0.30, 0.40

[a] For Groups 1 and 2 resonances. [b] For Group 3 resonances.

adiabatic cone V_u^{ad}

$$P_{u_\alpha}^{ad} = \sum_k |(F_{u_\alpha}^\theta | \chi_k^\theta)|^2 \times 100\% \qquad (21)$$

The c-product,[39] a generalized inner product, is used for the overlap (i.e., we do *not* complex conjugate the function $F_{u_\alpha}^\theta$). In determining $P_{u_\alpha}^{ad}$, it is necessary to use in the complex scaling computation of χ_k^θ the same rotation angle θ that was used in computing the resonance state eigenfunction $\Psi_{res_\alpha}^\theta$.

The percent population of resonance state α on the lower dissociative adiabat can be determined by computing the overlaps of $F_{l_\alpha}^\theta$ with *all* of the eigenfunctions of V_l^{ad}. Since overlaps with *both* continuum and resonance eigenfunctions of V_l^{ad} would be needed, it is much simpler to deduce this percent population from the value of $P_{u_\alpha}^{ad}$.

III. Resonance Results and Discussion

A. Resonance Energies. We focus on those resonances having positions $E_\alpha < 0.07$ au. We have successfully converged a total of 18 resonance energies; the resonances are equally divided into 3 groups based on their resonance width Γ_α (in atomic units)

Group 1: $\Gamma_\alpha/2 < 2.5 \times 10^{-4}$

Group 2: $5.0 \times 10^{-4} < \Gamma_\alpha/2 < 7.0 \times 10^{-4}$

Group 3: $\Gamma_\alpha/2 > 1.0 \times 10^{-3}$

The values of the numerical parameters used for the convergence of the resonance energies are listed in Table 3. The "production run" refers to those values used for calculating the resonance energies to be reported. The "convergence run" values were those used to check for convergence of the resonance energies. Notice that for convergence of the broad Group 3 resonances it is necessary to use a larger value for the rotation angle (0.35 rads) than is used (0.20 rads) for the narrower Groups 1 and 2 resonances. The value of the cutoff energy E_{cut} is approximately twice the value of 0.07 au used as the upper limit for resonance positions. Table 4 presents the resonance energies themselves in increasing order of E_α; we also give absolute uncertainties in E_α and percent uncertainties in Γ_α based on variations of the values of the numerical parameters. The lowest energy resonance, number 1, has a position lying below the conical intersection E_{CI}; it is extremely narrow and we can only obtain an order of magnitude estimate for its width numerically. The widths of the second narrowest resonance, number 13, and the broad resonance $\alpha = 16$, also have relatively large percent uncertainties. The positions E_α of the resonances are indicated in Figure 1 by solid lines, thicker dashed lines, and thickest long-dashed lines for Groups 1, 2, and 3, respectively. (Note that the placement of the horizontal lines representing the resonance positions is chosen only for convenience and that the resonances are not localized within the upper adiabatic potential.)

TABLE 4: Resonance Positions and Widths and Their Uncertainties[a]

resonance no.	group no.	E_α (E_h)	absolute uncertainty	$\Gamma_\alpha/2$ (E_h)	relative (%) uncertainty
1	1	1.162303 (−2)[b]	1. (−8)	1 (−9)[c]	c
2	1	1.9443 (−2)	2. (−6)	2.45 (−4)	0.5
3	2	2.609 (−2)	1. (−5)	6.28 (−4)	1.0
4	1	2.75758 (−2)	6. (−7)	9.07 (−5)	1.0
5	3	3.402 (−2)	1. (−5)	1.30 (−3)	2.0
6	1	3.61355 (−2)	7. (−7)	1.664 (−4)	0.5
7	1	4.1951 (−2)	4. (−6)	1.26 (−4)	2.5
8	3	4.204 (−2)	6. (−5)	1.64 (−3)	2.0
9	2	4.4758 (−2)	5. (−6)	5.37 (−4)	1.5
10	3	4.978 (−2)	7. (−5)	1.6 (−3)	6.5
11	2	5.121 (−2)	3. (−5)	6.35 (−4)	6.5
12	3	5.355 (−2)	2. (−5)	1.31 (−3)	2.5
13	1	5.704 (−2)	2. (−5)	7.6 (−5)	13
14	3	5.752 (−2)	3. (−5)	1.7 (−3)	6.0
15	2	6.016 (−2)	2. (−5)	6.09 (−4)	2.0
16	3	6.57 (−2)	5. (−4)	1.6 (−3)	12
17	2	6.585 (−2)	4. (−5)	5.9 (−4)	5.5
18	2	6.873 (−2)	3. (−5)	6.6 (−4)	1.5

[a] The uncertainties reflect tolerated changes in the resonance energies as numerical parameters are varied. [b] Read, for example, as $1.162\,303 \times 10^{-2}$. [c] Only an order of magnitude estimate for the width of this extremely narrow resonance could be obtained numerically.

Not listed in Table 4 is an apparent 19th resonance at $6.3 \times 10^{-2} - 2.6 \times 10^{-3}i$; this resonance is broader than all those listed in Table 4, and it was not particularly well-converged even with rotation angles ranging from 0.30 to 0.50 rads. We mention it here because we will allude to it in section IV. C.

The 18 resonance energies are clearly shown in the plot of the complex energy plane in Figure 2. The differing widths of the 3 groups are apparent in the Figure and sandwiched between Groups 2 and 3 are rotated continuum states. The two horizontal "lines" of continua eigenvalues are separated by ω_x and "within" a line, the eigenvalues are separated by ω_y.

It is strikingly apparent that there is no one-to-one correspondence between the positions and widths of the resonances; when the resonances are placed in increasing order of E_α, their corresponding widths (and therefore lifetimes) fluctuate irregularly. This is one of the dramatic effects of the presence of the conical intersection.

There is a close correspondence between the number of resonance states and the number of vibrational states $|n_x, m_y>$ below an energy of 0.07 au (see Table 2). This relationship will be fully analyzed in later discussions.

B. Resonance State Wave Functions: Diabatic Properties. The percent populations $P_b{}^d$ of the resonance states on the bound diabatic potential surface $V_b{}^d$ are shown in Figure 3. In general, we see that the narrower the resonance, the more it is "localized" on the bound diabatic PES. The narrow Group 1 resonances have at least 80% population on the bound diabat, as do the two lower energy resonances of Group 2. Even the higher energy Group 2 resonances have over 58% population on the bound diabat. This is in stark contrast to the higher energy broad Group 3 resonances; the last three-members of this group have less than 38% population on $V_b{}^d$.

The contributions from individual vibrational states $|n_x, m_y>$ of the bound diabat to the resonance states are very informative. Figure 4a−c displays $P_b^{n_x,m_y}$ for Groups 1, 2, and 3 resonances separately. We have only included states contributing at least 2% to the total diabatic resonance state wave function. Several trends are apparent. First, for Group 1 resonances, states with $n_x = 0$ or $m_y = 0$ make dominant contributions; this is in contrast to Group 3 where, for five of the six resonances, states with $n_x = 1$ dominate. Second, for a given resonance α, *all* vibrational

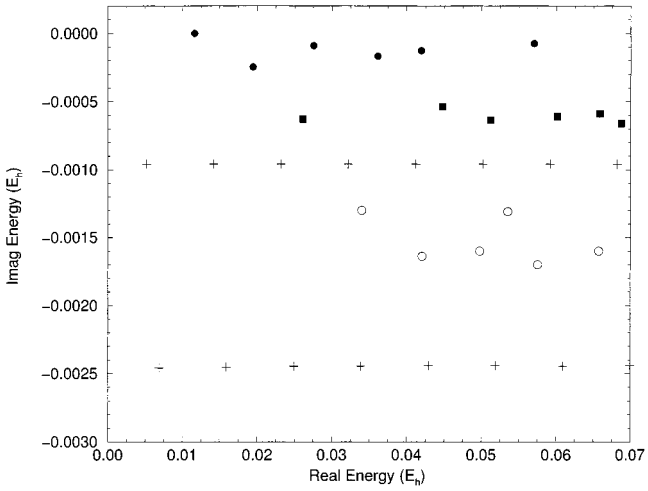

Figure 2. Real and imaginary parts of the complex eigenvalues for the conical intersection problem. The resonances of Groups 1, 2, and 3 are represented by darkened circles, squares, and open circles, respectively. The sets of rotated continua eigenvalues are indicated by plus signs.

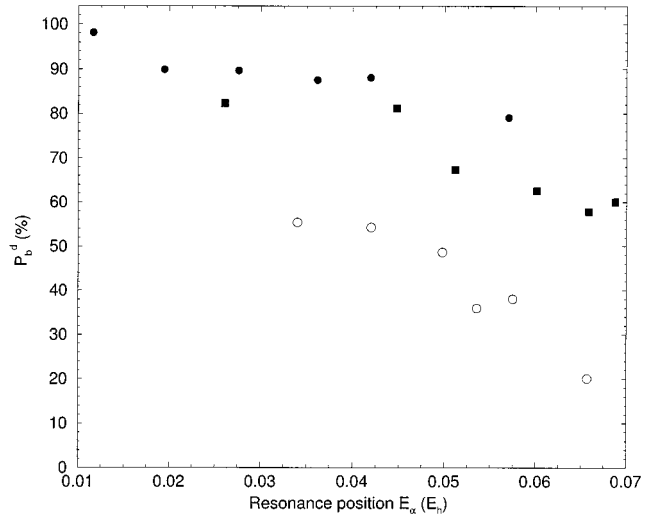

Figure 3. Populations $P_b{}^d$ of the resonances on the bound diabatic PES $V_b{}^d$. The resonances of Groups 1, 2, and 3 are represented by darkened circles, squares, and open circles, respectively.

states $|n_x, m_y>$ that contribute have *either* even values or odd values of m_y. This parity selection rule will be explained using symmetry considerations in section IV. A. Third, for resonances with close values of E_α, we often see a "switching" of the vibrational state making the dominant contribution. For example, consider the two resonances with positions near 0.027; for both resonance numbers 3 and 4, only $|0, 2>$ and $|1, 0>$ make significant contributions. For number 3, $|1, 0>$ contributes 67% and $|0, 2>$ contributes 13% whereas, for number 4, $|1, 0>$ contributes 20% and $|0, 2>$ contributes 69%. We should also note that the bound state energies of $|1, 0>$ and $|0, 2>$ (see Table 2) are close to E_α of 0.027 au. This "switching" of dominant contributors becomes even more apparent if we consider the percent contribution from an $|n_x, m_y>$ state relative to the total percent contribution from the bound diabat $V_b{}^d$; that is we define a relative percent contribution $R_{b_\alpha}^{n_x,m_y}$ via

$$R_{b_\alpha}^{n_x,m_y} = \frac{P_{b_\alpha}^{n_x,m_y}}{P_{b_\alpha}^{d}} \times 100\% \qquad (22)$$

In Table 5, we list clusters for the first 12 resonances

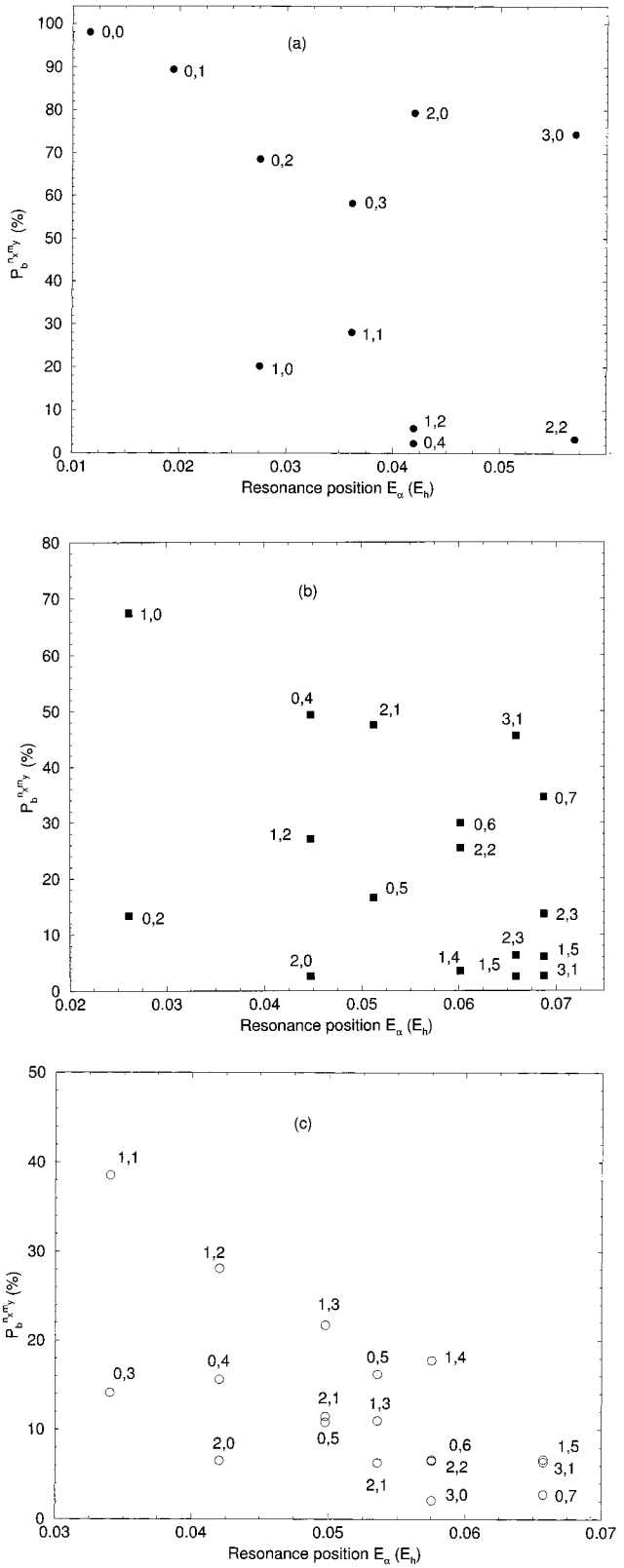

Figure 4. Contributions from individual vibrational levels $|n_x, m_y>$ of the bound diabat to the resonances. The points are labeled by n_x, m_y. (a) Group 1; (b) Group 2; (c) Group 3.

which have similar values of E_α and for which the same set of $|n_x, m_y>$ vibrational states contribute. The relative percent contributions $R_{b_\alpha}^{n_x,m_y}$ are tabulated. It is quite evident that this "switching" of dominant contributors is a recurring theme for the resonances; this "switching" behavior is not unique to the present study and is invariably observed when diagonalization

TABLE 5: Symmetry Groupings of Resonance States: Accurate Resonance Results (from complex scaling) versus Model Calculations (from H_R Diagonalization)

res. no.	sym. label	E_α[a] acc.[b]	E_α[a] mod.	$\Gamma_\alpha/2$ acc.[b]	$\Gamma_\alpha/2$ mod.	$\lvert n_x, m_y\rangle$	$R_b^{n_x,m_t}$ (%) acc.[c]	$R_b^{n_x,m_t}$ (%) mod.[d]
1	*A*	1.162303	1.164	1 (−9)[e]	0[f]	0,0	99.9	100[g]
2	*B*	1.9443	1.931	2.45 (−4)	3.12 (−4)	0,1	99.4	100[g]
3	*A*	2.609	2.636	6.28 (−4)	8.52 (−4)	1,0	82.0	73.8
						0,2	16.3	26.2
4	*A*	2.75758	2.788	9.07 (−5)	8.14 (−5)	1,0	22.5	26.2
						0,2	76.6	73.8
5	*B*	3.402	3.421	1.30 (−3)	1.75 (−3)	1,1	69.7	62.3
						0,3	25.5	37.7
6	*B*	3.61355	3.645	1.664 (−4)	7.94 (−5)	1,1	32.1	37.7
						0,3	66.5	62.3
7	*A*	4.1951	4.192	1.26 (−4)	2.42 (−5)	2,0	90.1	99.8
						1,2	6.6	
						0,4	2.6	0.2
8	*A*	4.204	3.699	1.64 (−3)	2.13 (−3)	2,0	12.0	0.1
						1,2	51.7	67.3
						0,4	28.7	32.6
9	*A*	4.4758	4.477	5.37 (−4)	1.94 (−4)	2,0	3.3	0.1
						1,2	33.4	32.7
						0,4	60.7	67.2
10	*B*	4.978	4.318	1.6 (−3)	2.86 (−3)	2,1	23.7	0.1
						1,3	44.7	67.1
						0,5	22.2	32.8
11	*B*	5.121	5.219	6.35 (−4)	3.73 (−4)	2,1	70.6	96.8
						1,3		0.6
						0,5	24.7	2.6
12	*B*	5.355	5.319	1.31 (−3)	2.65 (−4)	2,1	17.6	3.1
						1,3	30.6	32.0
						0,5	45.1	64.8

[a] Reported resonance positions have been multiplied by 100. [b] Taken from Table 4. [c] Contributions less than 2.5% not reported. [d] Contributions less than 0.1% not reported. [e] Read, for example, as 1×10^{-9}. [f] The H_R matrix of dimension 1 has no imaginary component. [g] H_R is of dimension 1.

of the Hamiltonian matrix mixes members of the basis sets. In section IV, we introduce an effective Hamiltonian whose analysis, using a simple model, will help us to understand (qualitatively and quantitatively) the results of Table 5.

We focused above on the contributions to the resonance state wave function from the vibrational states of the bound diabat V_b^d. Table 6 lists the percent contributions from a given vibrational state $|i_y>$ (in the *y*-dimension) of the dissociative diabat V_c^d where we have summed over the discrete set of continuum states (in the *x*-dimension); we only include contributions of 0.5% or greater. (We also show in Table 6 the total percent population P_c^d of the resonance state on the dissociative diabat.) The most obvious result is the opposite parity of $|m_y>$ and $|i_y>$; for example, if $|n_x, m_y>$ states from the bound diabat that contribute to the resonance all have even values of m_y, then the vibrational states $|i_y>$ of the dissociative diabat that contribute must be odd. This is easily understood; the diabatic coupling V_{bc}^d, being linear in *y*, is an *odd* function of *y*. Therefore, by symmetry, the matrix elements of the off-diagonal block of the complex scaled Hamiltonian $< n_x, m_y| V_{bc}^d| E_j, i_y >$ are nonvanishing only if $|m_y>$ and $|i_y>$ are of opposite parity.

The states of the diabatic potential surfaces V_b^d and V_c^d that are the dominant contributors to the diabatic resonance state wave functions are strikingly apparent in many of the surface plots of the amplitude-squared of $\Psi_{b_\alpha}^\theta$ and $\Psi_{c_\alpha}^\theta$. In Figures 5−9, we show surface plots for the diabatic resonance wave function components for selected resonances; the resonance wave functions shown have been normalized according to eq 11. For resonance number 1, $|\Psi_b^\theta|$ is remarkably similar to the $|n_x = 0, m_y = 0>$ wave function and $|\Psi_c^\theta|$ shows nodal structure in the *y*-direction of the $i_y = 1$ state. For resonance number 7, the nodal pattern of the $|2, 0>$ state appears in $|\Psi_b^\theta|$ and that of the $i_y = 1$ and $i_y = 3$ states appear in $|\Psi_c^\theta|$; the latter has a small magnitude since most of the population of this resonance resides on the bound diabatic surface. For resonance number 13, $|3, 0>$ dominates $|\Psi_b^\theta|$ and $|i_y = 1>$ dominates $|\Psi_c^\theta|$.

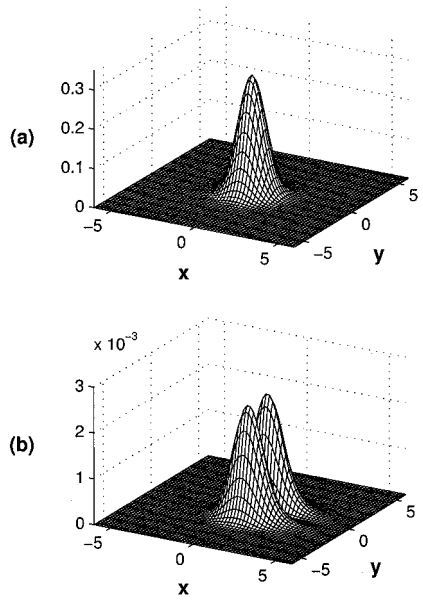

Figure 5. Surface plots of the amplitude-squared of the diabatic resonance state wave functions for resonance number 1: (a) $|\Psi_b^\theta|^2$; (b) $|\Psi_c^\theta|^2$.

As more and more states of V_b^d and V_c^d make significant contributions to the diabatic resonance state wave function, the

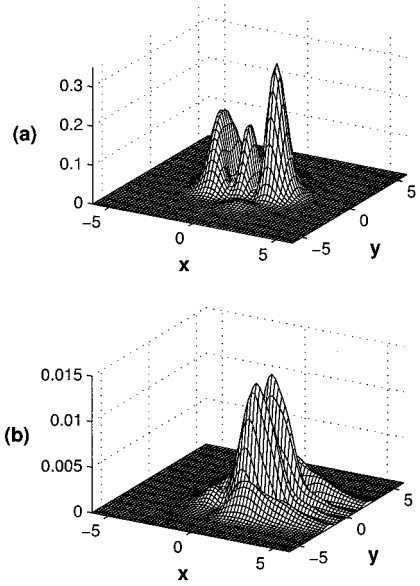

Figure 6. Surface plots of the amplitude-squared of the diabatic resonance state wave functions for resonance number 7: (a) $|\Psi_b^\theta|^2$; (b) $|\Psi_c^\theta|^2$.

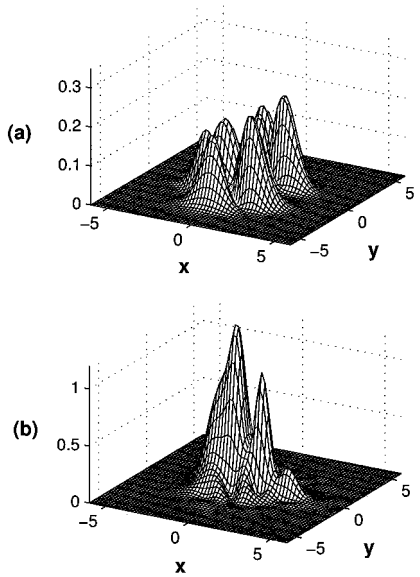

Figure 7. Surface plots of the amplitude-squared of the diabatic resonance state wave functions for resonance number 12: (a) $|\Psi_b^\theta|^2$; (b) $|\Psi_c^\theta|^2$.

surface plots become more and more complicated. For resonance number 12, it is hard to interpret the nodal structure in either component of the diabatic resonance wave function. For resonance number 17, although the nodal structure of $|3, 1>$ is apparent in $|\Psi_b^\theta|$, it is difficult to ascertain which $|i_y>$ states are contributing to Ψ_c^θ. However, the judicious choice of basis functions as described in section II allows us to immediately (and quantitatively) determine which vibrational states of both V_b^d and V_c^d contribute and we are not faced with the daunting task of trying to abstract this type of information from surface plots of the resonance wave functions.

C. Resonance State Wave Functions: Adiabatic Properties. Using the transformation described in section II.E, we computed adiabatic resonance state wave functions from the diabatic wave functions. In general, the adiabatic wave functions closely resemble the diabatic wave functions and therefore we do not show adiabatic wave function plots. At points (x, y) prior to the conical intersection, (i.e., $x < x_{CI}$)

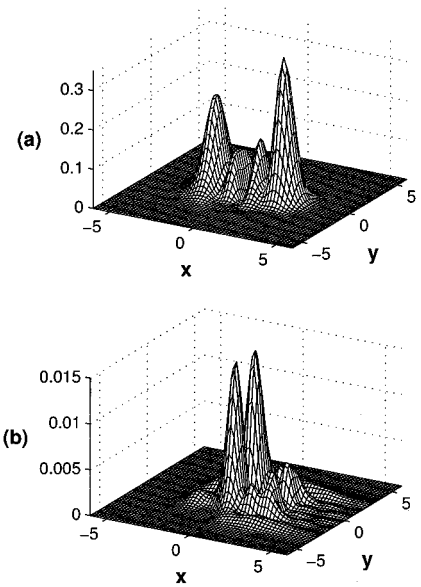

Figure 8. Surface plots of the amplitude-squared of the diabatic resonance state wave functions for resonance number 13: (a) $|\Psi_b^\theta|^2$; (b) $|\Psi_c^\theta|^2$.

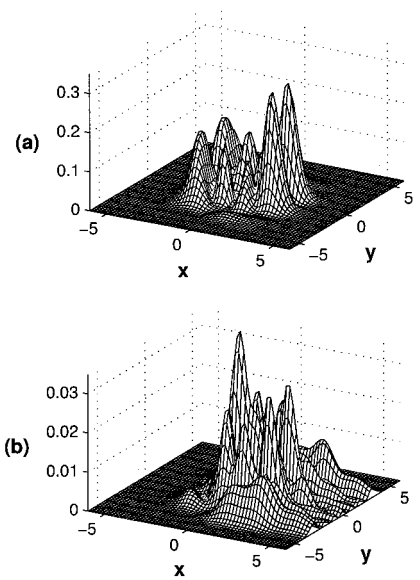

Figure 9. Surface plots of the amplitude-squared of the diabatic resonance state wave functions for resonance number 17: (a) $|\Psi_b^\theta|^2$; (b) $|\Psi_c^\theta|^2$.

$$|F_l^\theta| \approx |\Psi_b^\theta| \tag{23a}$$

and

$$|F_u^\theta| \approx |\Psi_c^\theta| \tag{23b}$$

whereas beyond the conical intersection, (i.e., $x > x_{CI}$)

$$|F_l^\theta| \approx |\Psi_c^\theta| \tag{23c}$$

and

$$|F_u^\theta| \approx |\Psi_b^\theta| \tag{23d}$$

A number of the resonance states display significant amplitudes for F_u^θ, indicating that there is significant population residing on the upper adiabat V_u^{ad}. Since the upper adiabatic PES is cone- or funnel-shaped and itself can support bound vibrational

TABLE 6: Populations of the Resonance State on the Dissociative Diabat and Contributions from Individual Vibrational States $|i_y>$ (summed over continuum states); for Example, Five Vibrational States $|i_y>$ of the Dissociative Diabat (with numbers *i* Given in Parentheses) Contribute Significantly to the 18th Resonance

res. no.	$P_c{}^d$ (%)			(i_y)	$P_c^{i_y}$ (%)		
1	1.9	(1)	1.9				
2	10.1	(0)	6.9	(2)	3.2		
3	17.7	(1)	16.9	(3)	0.7		
4	10.4	(1)	6.7	(3)	3.7		
5	44.6	(0)	12.9	(2)	29.9	(4)	1.8
6	12.5	(0)	4.1	(2)	4.2	(4)	4.1
7	12.0	(1)	8.0	(3)	3.7		
8	45.7	(1)	12.2	(3)	31.2	(5)	2.3
9	18.8	(1)	10.9	(3)	3.9	(5)	4.1
10	51.4	(0)	13.7	(2)	4.2	(4)	31.4
		(6)	2.0				
11	32.7	(0)	8.7	(2)	14.4	(4)	7.9
		(6)	1.7				
12	64.1	(0)	11.2	(2)	43.2	(4)	6.0
		(6)	3.6				
13	20.9	(1)	19.1	(3)	0.8	(5)	1.0
14	62.0	(1)	23.5	(3)	5.6	(5)	31.2
		(7)	1.5				
15	37.4	(1)	12.6	(3)	14.8	(5)	6.7
		(7)	3.3				
16	79.9	(0)	24.2	(2)	35.2	(4)	2.2
		(6)	17.1	(8)	0.8		
17	42.2	(0)	13.0	(2)	19.8	(4)	1.8
		(6)	7.3				
18	39.9	(0)	0.8	(2)	16.5	(4)	11.5
		(6)	6.8	(8)	4.3		

states, resonances with dominant $|F_u^\theta|$ may display behavior characteristic of "cone states".

For resonance number 1, the majority of the amplitude of the resonance state wave function is confined to a region of coordinate space prior to the conical intersection; it is not surprising that $|F_l^\theta|$ and $|\Psi_b^\theta|$ are extremely similar. In addition, as evidenced by the small magnitude of F_u^θ, there is little population of the adiabatic resonance state on the upper adiabatic PES; this is also to be expected since the $\alpha = 1$ resonance position falls below the conical intersection energy. For the other resonance states depicted in Figures 6 to 9, (i.e., $\alpha = 7$, 12, 13, 17), based on the magnitude of F_u^θ, we expect a significant contribution to the adiabatic resonance state wave function from the bound states of the V_u^{ad} adiabatic PES, with the largest contribution being made to the broad Group 3 resonance number 12.

The contributions from the states of the adiabatic PES to the adiabatic resonance state wave function can be quantified using eq 21. First, the bound states supported by the (uncoupled) adiabatic PES V_u^{ad} are computed without complex scaling (i.e., zero rotation angle) and the bound state energies are found to be converged to within 0.2% for various particle-in-a-box basis set parameters. The first 40 eigenstates are considered and, since their maximum eigenenergy is 0.132 au, these 40 states are expected to be sufficient for convergence of the sum needed in eq 21. (We also checked for convergence by considering only the first 32 of these eigenstates for the summation in eq 21.) With the exception of resonance number 12, there are no close matches (within 5×10^{-4} au or about 100 cm^{-1}) between the bound state eigenenergies and the resonance positions.

In computing the contributions from the V_u^{ad} bound states to resonances of Groups 1 and 2, we calculate χ_k^θ using $\theta = 0.20$ rads. The χ_k^θ have eigenenergies whose real parts are converged to within 0.5% when compared to the $\theta = 0$ eigenenergies. Similarly, for computing overlaps with the Group 3 adiabatic resonance state wave functions, we use $\theta = 0.35$ rads for determining χ_k^θ; the latter have real parts of their eigenenergies converged to within 7%. (The imaginary parts of the eigenenergies are nonzero due to the use of complex scaling but they are in general several orders of magnitude smaller than the real parts.) The overlaps between F_u^θ and χ_k^θ needed in eq 21 are computed using a two-dimensional Simpson's rule integrator. Results for P_u^{ad} are presented in Table 7; as the eigenfunctions χ_k^θ are more convergence-sensitive than their corresponding eigenenergies, it is difficult to provide uncertainties in these results. (We anticipate uncertainties in P_u^{ad} to be within a couple percent for Groups 1 and 2 but to be larger for Group 3.) The broad resonances of Group 3 tend to have relatively larger percent contributions from the upper adiabatic surface but numerous Group 1 and 2 resonances also have significant contributions. However, for none of the resonances is P_u^{ad} greater than 40% and, therefore, for none of the resonances is $|F_u^\theta|$ dominant.

TABLE 7: Populations of the Resonance State on the Upper Adiabatic Surface V_u^{ad} and the Eigenstate χ_k of V_u^{ad} of Maximum Contribution

resonance no. α	P_u^{ad} (%)	k	$\lvert Energy(\chi_k) - E_\alpha\rvert$ (cm^{-1})	contribution from χ_k (%)
1	2	2	6974	1
2	5	1	2951	2
3	12	5	7578	5
4	5	2	3473	2
5	27	1	248	7
6	13	1	712	9
7	28	2	318	13
8	28	2	298	7
9	21	2	298	16
10	28	3	187	7
11	30	4	505	13
12	40	4	9	16
13	26	5	786	14
14	15	19	919	3
15	21	6	733	10
16	33	26	10221	8
17	26	8	1003	6
18	20	8	371	7

We also report in Table 7 which eigenstate χ_k provides the largest contribution to P_u^{ad}. For all 18 resonances analyzed, the percent contribution from a specific adiabatic eigenstate to the resonance state never exceeds 20%; therefore, we can conclude that none of the resonances emanate from a specific adiabatic bound ("cone") state. Of all 18 resonances, number 12 has the largest contribution from bound states of the upper adiabatic PES; this is consistent with the close energy match (about 9 cm^{-1}) between E_{12} and the χ_4 eigenenergy. In fact, as seen in Table 7, one of the largest contributions from any one particular χ_k eigenstate is the 16% contribution to the adiabatic wave function of resonance number 12 from χ_4. However, for 10 of the 18 resonances, the largest contribution comes from an eigenstate χ_k whose bound state energy is *not* the closest one to the resonance position. Furthermore, as seen in Table 7, for all resonances α except number 12 the eigenstate χ_k which makes the largest contribution to P_u^{ad} has an energy at least 180 cm^{-1} away from the resonance position E_α.

The lower dissociative adiabatic PES V_l^{ad} can itself support resonance states and we have computed resonance energies using numerical parameters similar to those used for the 18 resonance states in Table 3. There is no apparent correlation between the resonance energies of V^d and those of V_l^{ad}; two of the resonance positions E_α of Table 4 are within 100 cm^{-1} of

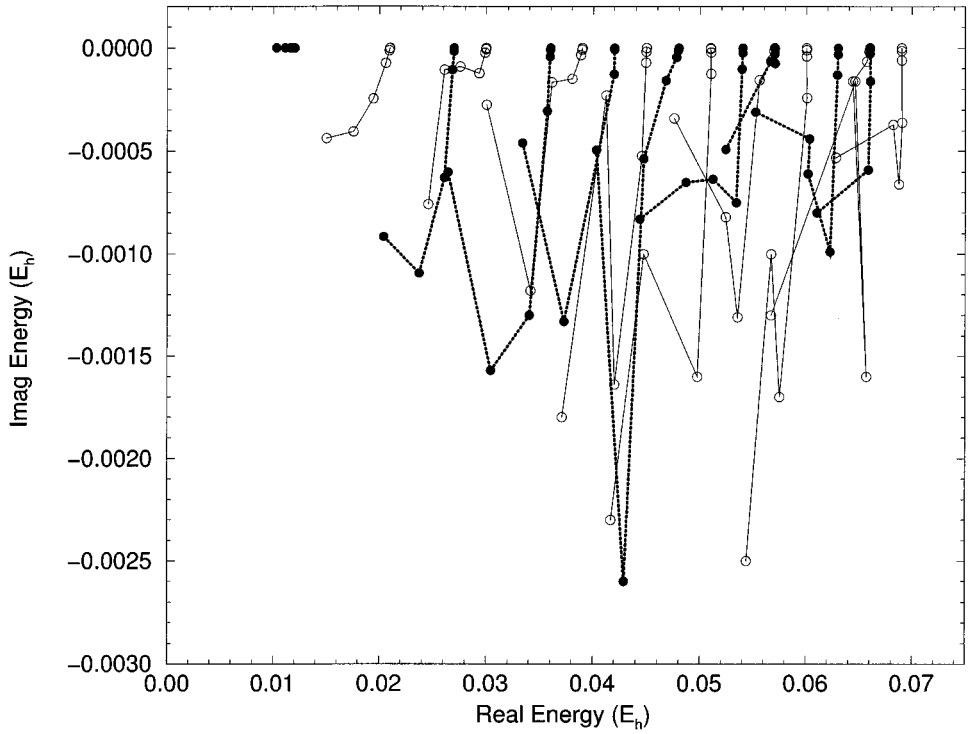

Figure 10. Variation of the resonance energies (including widths) with the nonadiabatic coupling strength. Shown are trajectories in the complex energy plane connecting the resonances for growing values of this coupling. The blackened circles (for odd-numbered resonances) and open circles (for even-numbered resonances) locate the computed resonance energies on the trajectories at values of the coupling strength of 0, 0.0005, 0.001, 0.0025, 0.005, 0.0075, and 0.01.

two of the positions of V_l^{ad} resonances but in both cases, the widths of the Table 4 resonance states are a factor of 5 larger than the widths of the resonances on the uncoupled lower adiabatic PES. The lowest energy resonance of V_l^{ad} has an energy of $0.0109-2 \times 10^{-4}i$; its resonance position is below the conical intersection energy E_{CI} but its width is much broader than resonance number 1 of Table 4. Therefore, the narrowness of resonance number 1 can *not* be attributed to the tunneling width on the lower adiabatic surface; the discussion presented in section IV.C gives an explanation for the narrowness of this resonance.

On the basis of the correspondence between the positions of the resonances in Table 4 and the vibrational states of the bound *diabatic* surface (see Figure 1 and discussion in section IV below) and the lack of correspondence between the former and the states of the (uncoupled) *adiabatic* potential surfaces, it appears that the diabatic representation gives a better zeroth order picture than does the adiabatic representation of the resonances arising from the conically intersecting electronic states. This zeroth order picture will prove useful in section IV where we show that numerous characteristics of the resonance states can be reproduced in at least a semiquantitative way using an effective Hamiltonian and a small subset of states of the diabatic potential surfaces.

D. Effect of Nonadiabatic Coupling Strength on Resonances. The results presented here thus far as well as those analyzed below in section IV are for a given set of potential parameters, in particular, a single value for the nonadiabatic coupling strength λ. We can also study the effects of the variation of λ on the resonance energies; the results of such a study are shown in Figure 10 for which we consider six different values of λ (0.0005, 0.001, 0.0025, 0.005, 0.0075, and 0.01). We have drawn "trajectories" connecting the resonance energies according to their numbering α using filled circles (odd α) and open circles (even α) to identify computed values along the trajectory. Each of the trajectories start at $\lambda = 0$, i.e., a diabatic vibrational energy level of Table 2. The doubly degenerate vibrational levels each split into two trajectories.

The first resonance changes little in energy and in particular in lifetime relative to changes for all other resonances. It appears that the diabatic approximation is a good zero order description in this case. The trajectory of resonance number 2 moves smoothly into the complex energy plane until the resonance position (0.015 02) is finally just slightly below the energy of the conical intersection; in fact, the resonance for the largest λ even overlaps the conical intersection if we consider its resonance width of 8.8×10^{-4}. For all the other resonances, the trajectories look more complicated. Up to about $\lambda = 0.0025$, the diabatic vibrational level is a reasonably good approximation for the resonance position. However, at larger λ, there are strong interactions between the modes; a single diabatic level (and, at least for $\lambda = 0.005$, a single adiabatic level) does not give a good zero order description for the resonance position. An analysis of the trajectories as a function of λ is not obvious and will be considered in future work. Increasing λ results in a decrease in the resonance position E_α and, in general, in a decrease in the resonance lifetime but there are numerous exceptions to the latter (see for example the third resonance). Many of the trajectories have a nonmonotonic behavior and the variation of the resonance energies with λ can be very abrupt and irregular for coupling strengths not close to zero. At large λ, the resonances might be thought of as resulting from a strong mixing of the resonances at smaller λ. The irregular behavior of the resonance energies (including lifetimes) as a function of the nonadiabatic coupling strength is a fingerprint of the conical intersection.

IV. Analysis of Resonance States

A. Symmetry Considerations. We have used symmetry arguments above in section III.B to explain why vibrational

states $|m_y>$ and $|i_y>$ associated with V_b^d and V_c^d, respectively, that contribute to a resonance state must be of opposite parity. Furthermore, we can easily show that if two vibrational states $|n_x', m_y'>$ and $|n_x, m_y>$ of the bound diabatic surface contribute to a resonance state then $|m_y>$ and $|m_y'>$ must be of the same parity. In fact, the resonances studied here can be classified by their vibronic symmetry; two symmetry classes are found and each class can be considered separately.

The Hamiltonian matrix $\mathbf{H}(x, y)$ of eq 4 is constructed within a basis of two diabatic electronic states Φ_b and Φ_c, whose nuclear Hamiltonians are H_b and H_c, respectively. The electronic states are of differing electronic symmetries; without loss of generality, we let Φ_b belong to the irreducible representation *A* and Φ_c belong to the irreducible representation *B*. Since the coupling V_{bc}^d between Φ_b and Φ_c only depends on the mode *y*, it follows that (asymmetric mode) *y* transforms as *B*; (symmetric mode) *x* transforms as *A*. (For a thorough discussion of symmetry considerations, see ref 2.)

The states $|n_x, m_y>$ of H_b and $|E_j, i_y>$ of H_c have *vibrational* symmetries *A* or *B* according to whether the number of quanta in the *y*-vibrational mode is even or odd, respectively; the symmetries of the bound vibrational states are indicated in Figure 1. Therefore, the resonances themselves can be classified according to the *vibronic* symmetries *A* and *B*. For example, *A* resonances can only have contributions from *A* vibrational states of electronic state Φ_b *and B* vibrational states of electronic state Φ_c. The resonances are thus divided into two symmetry groups and each group can be considered separately.

From above, we immediately conclude that $|m_y>$ from H_b and $|i_y>$ from H_c must be of opposite parity; this result has been observed in section III. B. In addition, we see that all vibrational states of H_b that contribute to a given resonance α must be of the same vibrational symmetry; this is precisely what was also observed in section III. B. In Table 5, as well as in Figure 1, we have labeled the resonances by their symmetry. We see that the positions of *A* and *B* symmetry resonances are well separated energetically for the present set of potential parameters (of Table 1). The first resonance is of *A* symmetry, the second of *B*, then a pair of *A* resonances followed by a pair of *B* resonances; from then on, resonances appear in triples of alternating symmetry. It is clear that symmetry is decisive for a detailed understanding of the resonance results.

Closer inspection of Figure 1 reveals that whereas four vibrational states $|n_x, m_y>$ make important contributions to the set of highest-energy resonances of *A* symmetry, only three resonances from the conical intersection study are listed. In the subsection below, we not only address this issue but we quantitatively interpret the results of Table 5 by invoking a simple model using an effective energy-dependent Hamiltonian.

B. An Effective, Energy-Dependent Hamiltonian. We reconsider the Hamiltonian of eq 4. We are interested in solving the matrix equation

$$\begin{pmatrix} H_b & V_{bc}^d \\ V_{bc}^d & H_c \end{pmatrix}\begin{pmatrix} \psi_b \\ \psi_c \end{pmatrix} = E\begin{pmatrix} \psi_b \\ \psi_c \end{pmatrix} \tag{24}$$

where ψ_b and ψ_c are the (noncomplex scaled) components of the nuclear wave function on the two diabatic surfaces. The states of H_c provide the continuum for the bound vibrational states of H_b which become resonances through the coupling V_{bc}^d.

Upon expanding eq 24 into two equations, solving for ψ_c in the second equation in terms of ψ_b, while adding $i0^+$ to the resolvent, and substituting the expression for ψ_c into the first equation, we obtain

$$H_R\,\psi_b = E\psi_b \tag{25}$$

where H_R is the effective, energy-dependent Hamiltonian describing the resonances in the vibrationally bound subspace of H_b

$$H_R = H_b + V_{bc}^d\,(E - H_c + i0^+)^{-1}\,V_{bc}^d \tag{26}$$

Solutions of eq 25 give the resonances; *E* is the complex resonance energy.

Since H_R is an effective Hamiltonian in the bound space of H_b, ψ_b is a square-integrable function. In the expressions that follow, we assume ψ_b is normalized, i.e., $<\psi_b|\psi_b> = 1$. The complex resonance energy *E* is given as $<\psi_b|\,H_R|\psi_b>$ or

$$E = <\psi_b|\,H_b|\psi_b> + <\psi_b|\,V_{bc}^d(E - H_c + i0^+)^{-1}V_{bc}^d|\psi_b> \equiv E_b + F_b(E) \tag{27}$$

E_b is a real number; since ψ_b is a component of the resonance state wave function and is an eigenfunction *not* of H_b but of H_R, E_b differs from E_{bnd} of eq 3 and Table 2. $F_b(E)$ is a complex function of energy *E*; it may be decomposed into its real and imaginary parts as

$$F_b(E) = \Delta_b(E) - \frac{i}{2}\,\Gamma_b(E) \tag{28}$$

where $\Delta_b(E)$ and $\Gamma_b(E)$ are called shift and width functions, respectively.

The term $F_b(E)$ of eq 27 can be further expressed by using the completeness relation of the set of eigenfunctions of H_c, whose eigenvalues we denote E_c. In section II.A, these eigenfunctions were denoted $|E_j, i_y>$; here we simply call them $|c>$

$$F_b(E) = \int\frac{|<\psi_b|V_{bc}^d|c>|^2}{E - E_c + i0^+}\,dc = P\int\frac{|<\psi_b|\,V_{bc}^d|\,c>|^2}{E - E_c}\,dc - \pi i\int|<\psi_b|V_{bc}^d|c>|^2\,\delta(E - E_c)\,dc \tag{29}$$

where *P* stands for the principal part of the integral. The latter expression can be simplified by introducing the density ρ_{Ec} of continuum states $|c>$ defined via

$$dc = \rho_{E_c}\,dE_c \tag{30}$$

so that

$$F_b(E) = P\int\frac{|<\psi_b|V_{bc}^d|c>|^2}{E - E_c}\,\rho_{E_c}\,dE_c - \pi i\,|<\psi_b|V_{bc}^d|c(E_c = E)>|^2\,\rho_E \tag{31}$$

Equating the imaginary parts of eqs 28 and 31, we obtain

$$\Gamma_b(E) = 2\pi|<\psi_b|V_{bc}^d|c(E_c = E)>|^2\,\rho_E \tag{32}$$

where the continuum state $|c>$ and its density of states are evaluated at the resonance energy *E*. Equation (32) is reminiscent of Fermi's golden rule but here the width function is energy-dependent and ψ_b is not a bound state eigenfunction of H_b.

The above discussion is general and provides a tool for analyzing resonances induced by conical intersections. In the following, we now show in the context of the present model how analysis of a simple matrix representation of H_R helps us interpret the resonance states. First, we denote Hamiltonians for harmonic oscillators in x and y as H_x and H_y, respectively, and the Hamiltonian for the dissociative exponential function in x as $\bar{H}_x$

$$H_x = T(x) + V_b^d(x, y=0) = -\frac{1}{2}\omega_x \frac{\partial^2}{\partial x^2} + \frac{1}{2}\omega_x x^2 \quad (33a)$$

$$H_y = T(y) + V_b^d(x=0, y) = -\frac{1}{2}\omega_y \frac{\partial^2}{\partial y^2} + \frac{1}{2}\omega_y y^2 \quad (33b)$$

$$\bar{H}_x = T(x) + V_c^d(x, y=0) = -\frac{1}{2}\omega_x \frac{\partial^2}{\partial x^2} + \epsilon\, e^{-\beta(x+\delta)} + \Delta \quad (33c)$$

Using the above definitions and eq 2, we can write the effective Hamiltonian as

$$H_R = H_x + H_y + \lambda^2 y\,(E - H_y - \bar{H}_x + i0^+)^{-1}\, y \quad (34)$$

Equation 34 sheds considerable light on the conclusion drawn at the end of section III.C that the diabatic representation gives a better zeroth order picture in this study of the resonances than does the adiabatic representation. Since $H_x + H_y$ equals H_b, the nuclear Hamiltonian for the bound diabatic state acts as a zeroth order Hamiltonian for H_R and the term in eq 34 proportional to λ^2 acts as a perturbation Hamiltonian. Therefore, the smaller is the magnitude of the perturbation, the closer is the correspondence between the positions of the resonances and the vibrational energy levels of the diabatic potential V_b^d; we also expect that smaller magnitudes of the perturbation Hamiltonian give rise to narrower (longer-lived) resonances since the imaginary part of the complex resonance energy arises from this λ^2 term.

H_R gives rise to a secular matrix in the harmonic basis of H_x and H_y which exhibits a relatively simple structure. The matrix elements of H_R within the basis $|n_x, m_y>$ take the form

$$< n_x', m_y'|H_R|n_x, m_y > = (E_{n_x} + E_{m_y})\delta_{m_y m_y'}\delta_{n_x n_x'} +$$

$$\frac{\lambda^2}{2}[(m_y+1)\delta_{m_y m_y'} + \sqrt{(m_y+1)(m_y+2)}\,\delta_{m_y' m_y+2}] \times < n_x'|(E - E_{m_y+1} - \bar{H}_x + i0^+)^{-1}|n_x > +$$

$$\frac{\lambda^2}{2}[m_y\delta_{m_y m_y'} + \sqrt{m_y(m_y-1)}\,\delta_{m_y' m_y-2}] \times < n_x'|(E - E_{m_y-1} - \bar{H}_x + i0^+)^{-1}|n_x > \quad (35)$$

where E_{n_x} and E_{m_y} are given in eq 3. We see immediately that the only nonvanishing matrix elements are those with $m_y' = m_y$ or $m_y' = m_y \pm 2$, in accordance with the conclusion drawn above that all vibrational states of H_b that contribute to a given resonance must be of the same vibrational symmetry.

In analogy to $F_b(E)$ defined above for the general Hamiltonian H_R in eq 27, we introduce

$$F_{n_x' n_x}(E) = < n_x'|(E - \bar{H}_x + i0^+)^{-1}|n_x > \quad (36)$$

which are related to the expansion functions of $F_b(E)$ along x alone. Each of the H_R matrix elements in eq 35 contains two elements of F which depend solely on the mode x except that the energy is shifted by the y-mode

$$< n_x', m_y'|H_R|n_x, m_y > = (E_{n_x} + E_{m_y})\delta_{m_y m_y'}\delta_{n_x n_x'} +$$

$$\frac{\lambda^2}{2}[(m_y+1)\delta_{m_y m_y'} + \sqrt{(m_y+1)(m_y+2)}\,\delta_{m_y' m_y+2}] \times F_{n_x' n_x}(E - E_{m_y+1}) +$$

$$\frac{\lambda^2}{2}[m_y\delta_{m_y m_y'} + \sqrt{m_y(m_y-1)}\,\delta_{m_y' m_y-2}]F_{n_x' n_x}(E - E_{m_y-1}) \quad (37)$$

Equation 37 is critical to using the effective Hamiltonian H_R to understand the structure of the resonances described in our system of conically intersecting states. The first term on the right-hand side of eq 37 gives rise to a diagonal matrix composed of the vibrational energy levels of the bound diabatic PES. The real parts of the second and third terms are responsible for the energy shifts of the resonance positions from the bound vibrational levels. The imaginary parts of $F_{n_x' n_x}(E - E_{m_y \pm 1})$ are responsible for the widths or lifetimes of the resonance states. We also reiterate that the $F_{n_x' n_x}$ functions are not evaluated at the resonance energy E but rather at $E - E_{m_y \pm 1}$; this is important because, as we shall show below, when the argument of $F_{n_x' n_x}$ has a negative real energy, then the imaginary part of $F_{n_x' n_x}$ will vanish. A given resonance may emanate primarily from a *single* $|n_x, m_y>$ state or from *multiple* vibrational states; in the latter case, only vibrational states with even (odd) values of m_y can couple to each other and diagonalization of the H_R matrix is necessary to find resonance energies.

The $F_{n_x' n_x}(E)$ terms are relatively straightforward to determine. Taking advantage of the completeness relation of the set of eigenfunctions $|E_j>$ of $\bar{H}_x$, whose density of states is denoted $\rho^x_{E_j}$, we obtain

$$F_{n_x' n_x}(E) = P\int \frac{< n_x'|E_j >< E_j|n_x >}{E - E_j}\,\rho^x_{E_j}\,dE_j - \pi i < n_x'|E_j(E) >< E_j(E)|n_x > \rho^x_E \quad (38)$$

where $|E_j(E)>$ is a continuum eigenfunction of $\bar{H}_x$ at energy E with density of states ρ^x_E.

To describe a resonance correctly, we need to decide how many $|n_x, m_y>$ states are needed for the secular determinant for H_R. We use the results in Table 5 as a guide; for examples, for the lowest energy resonances of A and B symmetry, the H_R matrix is of dimension one but for the highest energy resonances of both symmetries considered in Table 5, the H_R matrix is of dimension three. The effective Hamiltonian H_R is energy-dependent, but in our simple model we will diagonalize the H_R matrix at a single energy for each cluster of resonances shown in Table 5. When only one $|n_x, m_y>$ state contributes to a resonance, we simply take $E = E_{\mathrm{bnd}}$ where E_{bnd} is the vibrational energy given by eq 3. However, when two or more states contribute, we take E to be the average vibrational energy; for example, for the highest energy A resonances of Table 5, we set $E = 0.045$ (the average of the 0.042, 0.045, and 0.048 bound state energies) in evaluating $F_{n_x' n_x}(E - E_{m_y \pm 1})$.

To evaluate the terms in eq 38, we need to compute overlaps between vibrational states $|n_x>$ and continuum states $|E_j>$ as well as the density of continuum states. First, we obtain a discrete set of (real) continuum states and continuum energies

by diagonalizing $\bar{H}_x$ of eq 33c in a finite-size box using particle-in-a-box basis functions. (The continuum wave functions are the X_{2j}^{θ} functions of section II.C but with $\theta = 0$.) A set of 17 continuum states with an energy E_j up to 0.08 au is considered. (We also considered a set of 15 continuum states obtained from the use of a different particle-in-a-box basis. Similar results for diagonalization of H_R are obtained.) Second, we compute the density of states at each discrete energy E_j via[41]

$$\rho_{E_j}^{x} = \frac{1}{E_{j+1} - E_j} \tag{39}$$

To evaluate the imaginary part of $F_{n_x' n_x}(E)$ in eq 38, we need the density of continuum states at a specified energy, which is not in general one of the discretized energies. This density is obtained at an energy $E_j < E < E_{j+1}$ using a simple linear interpolation between $\rho_{E_j}^{x}$ and $\rho_{E_{j+1}}^{x}$.

Next, we compute the (real) harmonic oscillator states $|n_x>$ by diagonalizing H_x of eq 33a; these bound state wave functions are the $X_{1n}^{\theta=0}$ functions of section II.C and are obtained using the same particle-in-a-box basis functions as $X_{2j}^{\theta=0}$. The overlap $< n_x|\ E_j > = < X_{1n}^{\theta=0}|X_{2j}^{\theta=0} >$ is then computed numerically from the products of the expansion coefficients in the particle-in-a-box basis. The Franck−Condon factors for $n_x = 0$ and 1 are shown in Figure 11(a) and those for $n_x = 2$ and 3 in Figure 11b; the plots exhibit nodal structure analogous to the $|n_x>$ wave functions themselves. For the imaginary part of $F_{n_x' n_x}(E)$, we again use a simple linear interpolation, this time, for $E_j < E < E_{j+1}$, between the $| < n_x|E_j > |^2$ Franck−Condon factor and the $| < n_x|E_{j+1} > |^2$ Franck−Condon factor; then we use the square root of the resulting Franck−Condon factor for the off-diagonal elements of $F_{n_x' n_x}(E)$.

In eq 38 above, the real part of $F_{n_x' n_x}(E)$ involves the principal part of an integral which is evaluated by replacing the integral by a sum over the discrete continuum states and removing the density of states factor. (A similar type of procedure for the evaluation of an integral over continuum states is performed in ref 42.) In no cases are E and E_j very close to one another; the real part of $F_{n_x' n_x}$ reduces to

$$Re\ F_{n_x' n_x}(E) = \sum_j \frac{< n_x'|E_j > < E_j|n_x >}{E - E_j} \tag{40}$$

For each cluster of resonances, diagonalization of the H_R matrix at a single energy E yields (approximate) resonance eigenparameters; from the amplitude-squared of the complex eigenvectors, we obtain the percent contributions to the resonance state from the individual $|n_x, m_y>$ bound states. Since the secular H_R matrix is restricted to the subspace of the bound diabatic H_b, these percent contributions should be compared with the relative percent contributions $R_{b_\alpha}^{n_x, m_y}$ of eq 22 from the full (complex scaling) conical intersection study.

The crudeness of this model of analysis of the effective Hamiltonian H_R should be apparent. Nonetheless, for lower energy resonances, it works remarkably well. Since the effective Hamiltonian model begins to deteriorate for higher energy resonances, we only include in Table 5 results from the first 12 of the 18 resonances. For the higher energy resonances, it is likely that contributions from continuum states above 0.08 au would be necessary for more quantitative agreement. In light of the approximate nature of interpolated densities and Franck−Condon factors as well as the choice of a single value of energy for the energy-dependent H_R, we did not pursue the inclusion of higher energy continuum states.

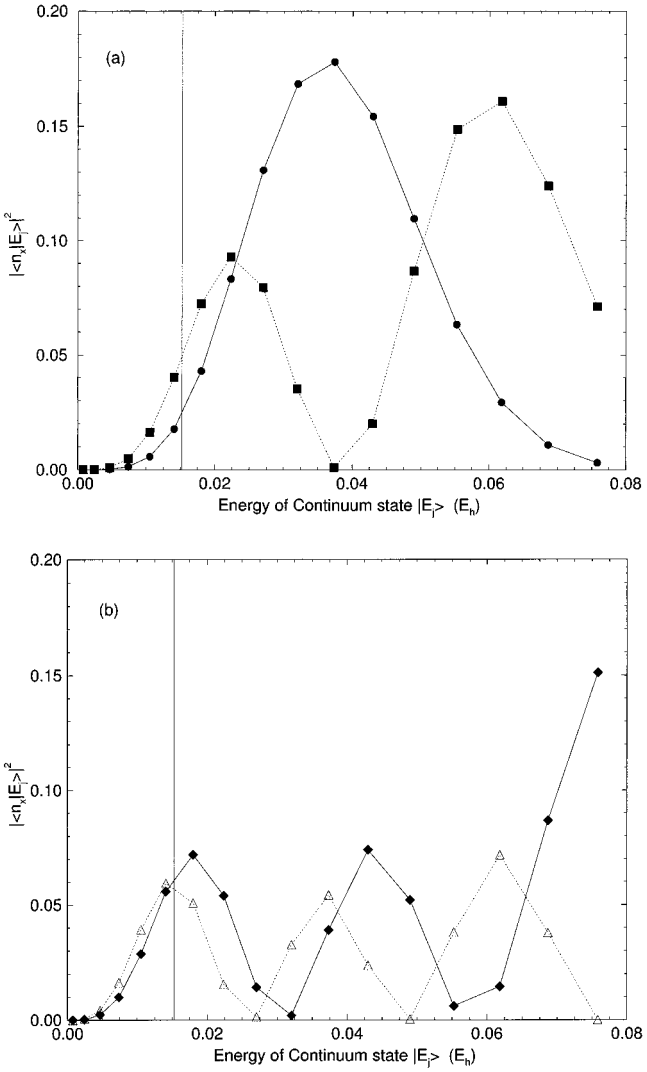

Figure 11. Franck−Condon factors between vibrational state $|n_x>$ of the bound diabat $V_b^d(x, y = 0)$ and the continuum state $|E_j>$ of the dissociative diabat $V_c^d(x, y = 0)$ at discrete continuum energies. A vertical line marks the conical intersection energy E_{CI}. (a) solid line (and circles) for $n_x = 0$; dotted line (and squares) for $n_x = 1$; (b) solid line (and diamonds) for $n_x = 2$; dotted line (and triangles) for $n_x = 3$.

C. Analysis of the Effective Hamiltonian: Results. Table 5 presents results from diagonalization of the H_R matrix in a basis of a limited number of $|n_x, m_y>$ states. We briefly describe key results. An underlying theme for all the resonances is that they can be characterized by a small number of vibrational states of the bound diabatic surface coupling to each other via the continuum of the dissociative diabatic surface.

1. Singlets of A and B Symmetries. The lowest energy resonance stems from the $|0, 0>$ vibrational level of H_b and is of A symmetry. Since the next lowest vibrational state of A symmetry (the $|1, 0>$ state) is far away energetically, only the element $< 0, 0|H_R|\ 0, 0 >$ has been considered; it is evaluated at the $|0, 0>$ vibrational energy $E_{bnd} = 0.012$ au. The real part of this matrix element is in excellent agreement with $E_{\alpha=1}$. Since, in eq 37, $E - E_{m_y+1} < 0$ and no continuum states $|E_j>$ exist at negative energies, the width Γ of the resonance is predicted to be zero. This explains why the lowest energy resonance of Table 4 and Figure 2 is very long-lived, i.e., very narrow. Numerically, the finite (but very small) width of $\alpha = 1$ comes from the weak coupling to higher vibrational levels of H_b. We also reiterate (see section III.C) that in the adiabatic picture it might be

tempting to associate this resonance width with regular tunneling through the lower adiabatic PES; however, the resonance lifetime is *much longer* (by about 5 orders of magnitude) than the tunneling lifetime.

The lowest energy resonance of *B* symmetry results from the $|0, 1>$ vibrational level of H_b. We only consider the element $< 0, 1|H_R|0, 1 >$ and its evaluation yields a resonance energy in good agreement with that of $\alpha = 2$.

2. Doublets of A and B Symmetries. Resonance numbers 3 and 4 of *A* symmetry arise primarily from the $|1, 0>$ and $|0, 2>$ vibrational levels of H_b, which are close together energetically. Since all other levels with an even number of *y*-quanta are far away energetically, we may restrict ourselves to an H_R matrix of dimension 2; we take energy $E = 0.0285$, the average of the two bound state energies. Table 5 shows that the results are in reasonable agreement. We successfully reproduce the "switching" of the dominant contributor described in section III. B. We also are able to explain the order of magnitude difference in the widths of the two resonances: that is, why one resonance is relatively short-lived and its partner relatively long-lived. This is the result of the two vibrational levels coupling to each other via the continuum; it is not due to one level coupling strongly to the continuum and the other level coupling weakly.

Resonance numbers 5 and 6 of *B* symmetry emanate mainly from the $|1, 1>$ and $|0, 3>$ vibrational levels of H_b and we diagonalized the 2×2 H_R matrix at $E = 0.0375$ au. The observations made above concerning the doublet of *A* symmetry are also applicable to the doublet of *B* symmetry.

3. Triplets of A and B Symmetries. Resonance numbers 7, 8, and 9 of *A* symmetry stem primarily from the $|2, 0>$, $|1, 2>$ and $|0, 4>$ vibrational levels of H_b and, as the next lowest vibrational level (the $|3, 0>$ level) is energetically far away, we took H_R to be of dimension 3 evaluated at the average bound state energy $E = 0.045$. We see from Table 5 that there is good agreement for two of the three resonance positions and the percent contributions to the resonance states from the $|n_x, m_y>$ levels are consistent. Diagonalization of H_R yields one broad and two narrower resonances as found in the full conical intersection study but the two narrower resonances have widths from H_R diagonalization that are factors of 3 to 5 too small.

Resonance numbers 10, 11, and 12 of *B* symmetry have contributions mainly from the $|2, 1>$, $|1, 3>$ and $|0, 5>$ vibrational states. As above for the *A* symmetry triplet, there is relatively good agreement for two of the three resonance positions, and we successfully predict which $|n_x, m_y>$ vibrational state is the dominant contributor to a given resonance. However, diagonalization of H_R yields one broad and two narrower resonances, inconsistent with the (observed) two broad and one narrow resonances; the approximate nature of the H_R analysis is becoming apparent at higher energies.

4. "Quartets" of A and B Symmetries. The highest energy clusters of resonances of *A* symmetry and of *B* symmetry appear in Figure 1 as triplets although four vibrational states $|n_x, m_y>$ in general make contributions to the resonance states (see for examples resonances 14 and 18 of Figure 4), and therefore, we would expect to observe two quartets of resonances in the complex scaling conical intersection study. As mentioned in section III.A, we did find an apparent 19th resonance at $6.3 \times 10^{-2} - 2.6 \times 10^{-3}i$ that was not very well-converged even with a variety of complex scaling rotation angles. It is likely that this very broad resonance is the fourth "missing" member of the quartet of *A* symmetry. As for the "missing" member of the *B* symmetry quartet, it should be kept in mind that we only sought converged resonances with $E_\alpha < 0.07$; it is possible that the position of the fourth resonance of the quartet exceeds this limit.

V. Concluding Remarks

We have presented an analysis of the resonance states that result from a conical intersection between a bound and a dissociative electronic state. Because this is the first such study of its kind to provide a detailed characterization of resonance energies (including lifetimes) and wave functions, we have focused on a two-coordinate system. The system under study models the simplest type of conical intersection, that which arises from two nondegenerate electronic states of different symmetries coupled via a nontotally symmetric normal-mode coordinate. This type of study is important for understanding the role of conical intersections in nonadiabatic effects, such as those accompanying the photodissociation of polyatomic molecules.

The complex resonance energies and eigenfunctions are computed using the complex coordinate method and a diabatic potential energy representation. The resonances arise from the vibrational states of the bound diabatic PES being predissociated via the nonadiabatic coupling to the dissociative diabatic PES. In fact, for calculational purposes, the bound and continuum states of the (uncoupled) diabatic potential energy surfaces are used as basis set functions for the resonance state wave function. This choice for the basis sets makes it very easy to compute the populations of the resonances on the diabatic surfaces as well as the percent contributions to the resonance eigenfunctions from individual vibrational levels of the diabatic surfaces.

A total of 18 resonances has been critically analyzed; they are equally divided into 3 groups on the basis of their resonance width. When the resonances are placed in increasing order of their resonance positions (i.e., the real parts of their complex resonance energies), we see that their widths fluctuate irregularly; there is no correspondence between the positions and lifetimes of the resonances. This is one of the dramatic effects of the presence of the conical intersection.

We have found that, in general, the narrower the resonance, the more it is localized on the bound diabatic PES. The very broad, high energy resonances have over 50% population on the dissociative diabatic PES. Upon calculating the contributions from individual vibrational levels of the bound diabatic PES, we observe, for resonances positioned close to each other, a "switching" of the vibrational state making the dominant contribution to the resonance. The states of the diabatic surfaces that are the dominant contributors are very apparent in many of the surface plots of the resonance eigenfunctions. However, as more and more diabatic surface vibrational states make significant contributions, the surface plots become more and more complicated.

The vibrational states of the bound diabat contributing to a given resonance state must have either even or odd values of the number of quanta in the unsymmetric normal mode. Furthermore, the states of the dissociative diabat that contribute to a given resonance must have opposite parity to the vibrational states of the bound diabat. These observations are easily explained in terms of the vibronic symmetries of the resonances themselves and we are able to divide the resonances into two symmetry classifications, *A* and *B*. The positions of the *A* and *B* symmetry resonances are well separated energetically. The first resonance is of *A* symmetry, followed by one of *B*, then a pair of *A* followed by a pair of *B*; thereafter, resonances appear in triples of alternating symmetry. It is clear that symmetry is critical for a detailed understanding of the resonances.

Although the resonance wave functions have been computed using the diabatic representation, we are also able to discuss the resonances in connection with adiabatic PES; this is done by projecting the computed resonance eigenfunctions in the diabatic representation on the adiabatic electronic states. We have computed the population of the resonance state on the upper adiabatic (cone) PES as well as the percent contributions from individual bound states of the upper adiabatic surface. The lowest energy resonance, whose position falls below the conical intersection, has very little population on the upper adiabatic PES, as is expected. The broad resonances tend to have a significant population on the upper adiabatic cone but a number of the narrower resonances do as well. However, none of the resonances analyzed emanate from a specific adiabatic bound (cone) state.

The lower dissociative adiabatic potential surface can itself (i.e., in the absence of potential coupling) support resonance states but we have found no apparent correlation between the resonance energies of the dissociative adiabatic PES and the resonance energies of the conically intersecting system. In particular, the lowest energy resonance of the dissociative adiabat has a width that is many orders of magnitude larger than the lowest energy resonance in the conical intersection study. Thus, the long lifetime of the latter resonance is not attributed to a tunneling lifetime on the lower adiabatic surface but rather is observed to be another dramatic effect of the presence of the conical intersection. This phenomenon is generic to conical intersections and deserves a special study.

We successfully have explained the long lifetime of this lowest energy resonance, as well as many other features of the resonance results, by introducing an effective Hamiltonian H_R which describes the resonances in the vibrationally bound subspace of the bound diabatic PES. The introduction of H_R sheds light on the observation that the diabatic representation provides a better zeroth order picture than the adiabatic representation for the resonances characterized in detail in this conical intersection study.

We have shown how, with the aid of H_R, a simple model can be derived which provides an effective tool for analyzing resonances induced by conical intersections. The analysis utilizing H_R shows that the resonances can be characterized by a small number of vibrational states of the bound diabat which couple to each other via the continuum of the dissociative diabat. For example, for the doublet of A (B) symmetry, that one resonance is long-lived and its partner short-lived is seen to be the result of the two vibrational levels coupling to each other via the continuum; it is not due to one level coupling strongly to the continuum and the other level weakly. We have provided explanations why, for the highest energy A and B symmetry resonances, only triplets of resonances have been identified, rather than a pair of quartets. For the A symmetry cluster, the missing member is likely to be a very broad resonance which we tentatively have identified in the conical intersection study as a 19th resonance. For the B symmetry cluster, the missing member quite possibly has a resonance position outside of the energy range of interest of this study.

Although we have concentrated here on a given set of potential parameters and a particular value for the nonadiabatic coupling strength λ, we also briefly investigated the effects of the variation of λ on the resonance energies. The irregular variation of the resonance energies with the coupling strength is a result of the conical intersection.

This is the first study of its kind to provide a detailed characterization of the resonance states induced by a conical intersection between a bound and a dissociative electronic state. The potential energy matrix used in the present study is applicable to realistic systems and can be generalized to more than two dimensions.

Acknowledgment. Acknowledgment is made to the donors of the Petroleum Research Fund, administered by the American Chemical Society, for partial support of this research. This work was also supported by an Indiana University Purdue University Fort Wayne Summer Faculty Research Grant, by the Israel-US Binational Science Foundation, by the Israel Academy of Science and Humanities, by the Fund of promotion of research at the Technion, and by Fonds der Chemischen Industrie.

References and Notes

(1) Born, M.; Oppenheimer, R. *Ann. Physik* (Leipzig) **1927**, *84*, 457.

(2) Köppel, H.; Domcke, W.; Cederbaum, L. S. *Adv. Chem. Phys.* **1984**, *57*, 59. Domcke, W.; Stock, G. *Adv. Chem. Phys.* **1997**, *100*, 1.

(3) Michl, J.; Bonačić-Koutecký, V. *Electronic Aspects of Organic Photochemistry*; John Wiley & Sons: New York, 1990.

(4) Bernardi, F.; Olivucci, M.; Robb, M. A. *Chem. Soc. Rev.* **1996**, 321.

(5) Yarkony, D. R. *J. Phys. Chem.* **1996**, *100*, 18 612. Yarkony, D. R. *Acc. Chem. Res.* **1998**, *31*, 511. Yarkony, D. R. *J. Phys. Chem. A* **2001**, *105*, 6277.

(6) Butler, L. J. *Annu. Rev. Phys. Chem.* **1998**, *49*, 125.

(7) Zhu, C.; Nakamura, H. *J. Chem. Phys.* **1994**, *101*, 10 630. Nakamura, H. *Annu. Rev. Phys. Chem.* **1997**, *48*, 299. Zhu, C.; Nakamura, H. *J. Chem. Phys.* **1997**, *106*, 2599. Zhu, C.; Nakamura, H.; Nobusada, K. *Phys. Chem. Chem. Phys.* **2000**, *2*, 557.

(8) Zener, C. *Proc. R. Soc.* (London) **1932**, *137A*, 696. Landau, L. D. *Phys. Z. Sowjetunion* **1932**, *2*, 46.

(9) Shin, S.; Light, J. C. *J. Chem. Phys.* **1994**, *101*, 2836. Qi, J.; Bowman, J. M. *J. Chem. Phys.* **1996**, *104*, 7545. Friedman, R. S.; Allison, T. C.; Truhlar, D. G. *Phys. Chem. Chem. Phys.* **1999**, *1*, 1237. Friedman, R. S.; Ryaboy, V. M.; Moiseyev, N. *J. Chem. Phys.* **1999**, *111*, 7187.

(10) Zhu, C.; Nikitin, E. E.; Nakamura, H. *J. Chem. Phys.* **1996**, *104*, 7059. Nikitin, E. E. *J. Chem. Phys.* **1997**, *107*, 6748. Alijah, A.; Nikitin, E. E. *Mol. Phys.* **1999**, *96*, 1399.

(11) Köppel, H.; Cederbaum, L. S.; Domcke, W. *J. Chem. Phys.* **1988**, *89*, 2023. Döscher, M.; Köppel, H. *Chem. Phys.* **1997**, *225*, 93. Koizumi, H.; Bersuker, I. B.; Boggs, J. E.; Polinger, V. Z. *J. Chem. Phys.* **2000**, *112*, 8470.

(12) Salzgeber, R. F.; Mandelshtam, V. A.; Schlier, Ch.; Taylor, H. S. *J. Chem. Phys.* **1999**, *110*, 3756. Santoro, F.; Petrongolo, C. *J. Chem. Phys.* **1999**, *110*, 4419. Santoro, F.; Petrongolo, C.; Granucci, G.; Persico, M. *Chem. Phys.* **2000**, *259*, 193. Santoro, F.; Petrongolo, C.; Granucci, G.; Persico, M. *Chem. Phys.* **2000**, *261*, 489. Santoro, F.; Petrongolo, C.; Lami, A. *J. Chem. Phys.* **2000**, *113*, 4073. Mahapatra, S.; Köppel, H.; Cederbaum, L. S.; Stampfuss, P.; Wenzel, W. *Chem. Phys.* **2000**, *259*, 211.

(13) Smalley, R. E.; Wharton, L.; Levy, D. H. *J. Chem. Phys.* **1975**, *63*, 4977. Biesheuvel, C. A.; Bulthuis, J.; Janssen, M. H. M.; Stolte, S.; Snijders, J. G. *J. Chem. Phys.* **2000**, *112*, 3633, and references therein. Heilliette, S.; Delon, A.; Dupré, P.; Jost, R. *Phys. Chem. Chem. Phys.* **2001**, *3*, 2268.

(14) Raab, A.; Worth, G. A.; Meyer, H.-D.; Cederbaum, L. S. *J. Chem. Phys.* **1999**, *110*, 936.

(15) Zimmermann, Th.; Köppel, H.; Cederbaum, L. S. *J. Chem. Phys.* **1989**, *91*, 3934.

(16) Biesner, J.; Schneider, L.; Ahlers, G.; Xie, X.; Welge, K. H.; Ashfold, M. N. R.; Dixon, R. N. *J. Chem. Phys.* **1989**, *91*, 2901. Waschewsky, G. C. G.; Kitchen, D. C.; Browning, P. W.; Butler, L. J. *J. Phys. Chem.* **1995**, *99*, 2635. Forde, N. R.; Morton, M. L.; Curry, S. L.; Wrenn, S. J.; Butler, L. J. *J. Chem. Phys.* **1999**, *111*, 4558. Forde, N. R.; Butler, L. J.; Ruscic, B.; Sorkhabi, O.; Qi, F.; Suits, A. *J. Chem. Phys.* **2000**, *113*, 3088. Reid, J. P.; Loomis, R. A.; Leone, S. R. *J. Phys. Chem. A* **2000**, *104*, 10 139.

(17) Person, M. D.; Kash, P. W.; Butler, L. J. *J. Chem. Phys.* **1992**, *97*, 355. Kash, P. W.; Waschewsky, G. C. G.; Butler, L. J.; Francl, M. M. *J. Chem. Phys.* **1993**, *99*, 4479. Waschewsky, G. C. G.; Kash, P. W.; Myers, T. L.; Kitchen, D. C.; Butler, L. J. *J. Chem. Soc., Faraday Trans.* **1994**, *90*, 1581.

(18) Myers, T. L.; Forde, N. R.; Hu, B.; Kitchen, D. C.; Butler, L. J. *J. Chem. Phys.* **1997**, *107*, 5361.

(19) Amaral, G.; Xu, K.; Zhang, J. *J. Phys. Chem. A* **2001**, *105*, 1465.

(20) Parsons, B. F.; Curry, S. L.; Mueller, J. A.; Ray, P. C.; Butler, L. J. *J. Chem. Phys.* **1999**, *111*, 8486. Mueller, J. A.; Morton, M. L.; Curry, S. L.; Abbatt, J. P. D.; Butler, L. J. *J. Phys. Chem. A* **2000**, *104*, 4825.

(21) Guo, H. *J. Chem. Phys.* **1992**, *96*, 2731, 6629. Jung, Y.-J.; Park, M. S.; Kim, Y. S.; Jung, K.-H. *J. Chem. Phys.* **1999**, *111*, 4005. Zou, P.; McGivern, W. S.; North, S. W. *Phys. Chem. Chem. Phys.* **2000**, *2*, 3785. Xie, D.; Guo, H.; Amatatsu, Y.; Kosloff, R. *J. Phys. Chem. A* **2000**, *104*, 1009. Park, M. S.; Kim, T. K.; Lee, S.-H.; Jung, K.-H.; Volpp, H.-R.; Wolfrum, J. *J. Phys. Chem. A* **2001**, *105*, 5606. Arnold, P. A.; Cosofret, B. R.; Dylewski, S. M.; Houston, P. L.; Carpenter, B. K. *J. Phys. Chem. A* **2001**, *105*, 1693.

(22) Castle, K. J.; Abbott, J.; Peng, X.; Kong, W. *Chem. Phys. Lett.* **2000**, *318*, 565.

(23) Trushin, S. A.; Fuss, W.; Kompa, K. L.; Schmid, W. E. *J. Phys. Chem. A* **2000**, *104*, 1997. Trushin, S. A.; Fuss, W.; Schmid, W. E. *Chem. Phys.* **2000**, *259*, 313.

(24) Harrevelt, R. van; Hemert, M. C. van *J. Chem. Phys.* **2000**, *112*, 5777, 5787. Harich, S. A.; Hwang, D. W. H.; Yang, X.; Lin, J. J.; Yang, X.; Dixon, R. N. *J. Chem. Phys.* **2000**, *113*, 10 073. Harich, S. A.; Yang, X.; Hwang, D. W. H.; Lin, J. J.; Yang, X.; Dixon, R. N. *J. Chem. Phys.* **2001**, *114*, 7830.

(25) Baumert, T.; Herek, J. L.; Zewail, A. H. *J. Chem. Phys.* **1993**, *99*, 4430.

(26) Costen, M. L.; North, S. W.; Hall, G. E. *J. Chem. Phys.* **1999**, *111*, 6735. Coronado, E.; Batista, V. S.; Miller, W. H. *J. Chem. Phys.* **2000**, *112*, 5566.

(27) Manaa, M. R. *J. Chem. Phys.* **2000**, *112*, 8789.

(28) Hoffman, B. C.; Yarkony, D. R. *J. Chem. Phys.* **2000**, *113*, 10 091.

(29) Votava, O.; Plusquellic, D. F.; Myers, T. L.; Nesbitt, D. J. *J. Chem. Phys.* **2000**, *112*, 7449.

(30) Conroy, D.; Aristov, V.; Feng, L.; Reisler, H. *J. Phys. Chem. A* **2000**, *104*, 10 288.

(31) Blanchet, V.; Stolow, A. *J. Chem. Phys.* **1998**, *108*, 4371.

(32) Schinke, R.; Bittererová, M. *Chem. Phys. Lett.* **2000**, *332*, 611. Yarkony, D. R. *J. Chem. Phys.* **2001**, *114*, 2614.

(33) Flöthmann, H. F.; Beck, C.; Schinke, R.; Woywod, C.; Domcke, W. *J. Chem. Phys.* **1997**, *107*, 7296. Batista, V. S.; Miller, W. H. *J. Chem. Phys.* **1998**, *108*, 498.

(34) Kroes, G.-J.; Hemert, M. C. van; Billing, G. D.; Neuhauser, D. *J. Chem. Phys.* **1997**, *107*, 5757. Kroes, G.-J.; Hemert, M. C. van; Billing, G. D.; Neuhauser, D. *Chem. Phys. Lett.* **1997**, *271*, 311.

(35) Simah, D.; Hartke, B.; Werner, H.-J. *J. Chem. Phys.* **1999**, *111*, 4523.

(36) Manthe, U.; Köppel, H.; Cederbaum, L. S. *J. Chem. Phys.* **1991**, *95*, 1708.

(37) Atabek, O.; Lefebvre, R. *J. Chem. Phys.* **1992**, *97*, 3973.

(38) Manthe, U.; Köppel, H. *J. Chem. Phys.* **1990**, *93*, 1658.

(39) Moiseyev, N. *Phys. Reports* **1998**, *302*, 211.

(40) Bar-On, I.; Ryaboy, V. *Siam J. Sci. Comput.* **1997**, *18*, 1412.

(41) Alon, O. E.; Moiseyev, N. *Phys. Rev. A* **1992**, *46*, 3807.

(42) Moiseyev, N.; Santra, R.; Zobeley, J.; Cederbaum, L. S. *J. Chem. Phys.* **2001**, *114*, 7351.